Interaction of a Tunnel-like Acoustic Disturbance Field with a Blunt Cone Boundary Layer at Mach 8

Yuchen Liu*, Mateus Schuabb† and Lian Duan‡
The Ohio State University, Columbus, OH 43210, USA

Pedro Paredes§
National Institute of Aerospace, Hampton, VA 23666, USA

Meelan M. Choudhari¶
NASA Langley Research Center, Hampton, VA 23681, USA

The existing measurements of laminar-to-turbulent transition over circular cones in conventional (i.e., "noisy") hypersonic wind tunnels have established that the transition location moves downstream when the nose radius is increased from zero. However, this initially downstream movement slows down and ultimately reverses beyond a critical value of the nose radius, and may be related to external forcing in the form of freestream disturbances and/or surface roughness. To understand the effects of freestream acoustic disturbances on transition reversal over a blunt body, hypersonic boundary-layer receptivity to broadband freestream acoustic disturbances from the nozzle wall of a digital conventional wind tunnel is investigated by both direct numerical simulations (DNS) and modal and nonmodal stability analysis. A Mach 8 flow over a 7 deg half-angle cone with a nose radius of $R_n = 5.2$ mm and freestream unit Reynolds number of 12.2×10^6 m^{-1} is considered. The results show that the broadband tunnel noise in the free stream of a convectional hypersonic wind tunnel (i.e., outside the nozzle-wall turbulent boundary layer) can be well represented by an acoustic model with an ansatz of slow plane acoustic waves. With successful calibration of the model parameters against the precursor tunnel DNS, such an acoustic ansatz can successfully reproduce both the frequency-wavenumber spectra and the temporal evolution of the broadband tunnel noise radiated from the nozzle wall. Additionally, the DNS of the Mach 8 blunt cone with tunnel-like acoustic input above the bow shock showed that the spectra of wall-pressure and heat-transfer fluctuations recover the signature of the axisymmetric waves predicted by the nonmodal analysis. Furthermore, the azimuthal wavenumber and frequency spectrum of the temperature fluctuations as a function of the wall-normal distance show higher amplitudes for three-dimensional waves above the boundary-layer edge. The numerical schlieren contours show the inclined structures commonly observed in blunt cone experiments, demonstrating that they correspond to three-dimensional structures due to freestream disturbances in the presence of an entropy layer.

Nomenclature

C_f	=	Skin friction coefficient, $C_f = \tau_w/(0.5\rho_\infty U_\infty^2)$, dimensionless
C_p	=	heat capacity at constant pressure, J/(K·kg)
C_v	=	heat capacity at constant volume, J/(K·kg)
E	=	total energy norm, J
f	=	frequency, Hz
H	=	shape factor, $H = \delta^*/\theta$, dimensionless
h_ξ	=	streamwise metric factor

*Graduate Student, Department of Mechanical and Aerospace Engineering
†Graduate Student, Department of Mechanical and Aerospace Engineering
‡Associate Professor, Department of Mechanical and Aerospace Engineering, Associate Fellow, AIAA
§Senior Research Engineer, Computational AeroSciences Branch, NASA LaRC. Senior Member, AIAA
¶Aerospace Technologist, Computational AeroSciences Branch, M.S. 128. Fellow, AIAA

h_ζ = spanwise metric factor, m
J = objective function
M = Mach number, dimensionless
m = azimuthal wavenumber, rad^{-1}
N = Logarithmic amplification factor
$\hat{\mathbf{q}}$ = vector of amplitude variables
$\check{\mathbf{q}}$ = vector of disturbance function variables
$\bar{\mathbf{q}}$ = vector of base flow variables
$\tilde{\mathbf{q}}$ = vector of perturbation variables
Pr = Prandtl number, $Pr = 0.71$, dimensionless
R = ideal gas constant, J/(K·kg)
Re_∞ = freestream unit Reynolds number, $Re_u = \rho_{1,\infty} U_{1,\infty}/\mu_{1,\infty}$, m^{-1}
Re_θ = Reynolds number based on momentum thickness and freestream viscosity, $Re_\theta = \rho_{2,\infty} U_{2,\infty}\theta/\mu_{2,\infty}$, dimensionless
Re_{δ_2} = Reynolds number based on momentum thickness and wall viscosity, $Re_{\delta 2} = \rho_{2,\infty} U_{2,\infty}\theta/\mu_w$, dimensionless
Re_τ = Reynolds number based on friction velocity and wall viscosity, $Re_\tau = \rho_w u_\tau \delta/\mu_w$, dimensionless
R_n = cone nose radius, mm
S = entropy, $S = \frac{\gamma}{\gamma-1}\ln\frac{T}{T_{1,\infty}} - \ln\frac{p}{p_{1,\infty}}$, dimensionless
T = temperature, K
T_r = recovery temperature, $T_r = T_{1,\infty}[1 + 0.89 * (\gamma - 1)M^2_{1,\infty}/2]$, K
U = mean streamwise velocity in the local body intrinsic coordinate system, m/s
c = speed of sound, m/s
p = pressure, Pa
q = dynamic pressure, Pa
r = radial coordinate
u = streamwise velocity in the right hand Cartesian coordinate, m/s
u_τ = friction velocity, $u_\tau \equiv \tau_w/\overline{\rho}_w$, m/s
v = spanwise velocity in the right hand Cartesian coordinate, m/s
w = vertical velocity in the right hand Cartesian coordinate, m/s
x = streamwise direction of the right hand Cartesian coordinate, m
y = spanwise direction of the right hand Cartesian coordinate, m
z = vertical coordinate that is perpendicular to the plane determined by the x- and y-coordinates, m
z_n = wall-normal direction of the local body intrinsic coordinate system, m
z_τ = viscous length, $z_\tau = \nu_w/u_\tau$, m
γ = specific heat ratio, $\gamma = C_p/C_v$, dimensionless
δ = boundary layer thickness (based on 99.5% of the total enthalpy), m
δ^* = displacement thickness, m
κ = thermal conductivity, $\kappa = \mu C_p/Pr$, W/(m·K)
θ = momentum thickness, m
μ = dynamic viscosity, kg/(m·s)
ν = kinematic viscosity, $\nu = \mu/\rho$, m^2·s
ρ = density, kg/m^3
τ_w = wall shear stress, Pa

Subscripts

e = boundary-layer edge variables
i = inflow station for the domain of direct numerical simulations
o = stagnation quantities
rms = root mean square
w = wall quantities
$1, \infty$ = freestream quantities before the shock of the cone
$2, \infty$ = freestream quantities behind the shock but outside of the boundary layer of the cone

Superscripts

$+$ = inner wall units
$\overline{(\cdot)}$ = statistically averaged variables

$(\cdot)'$ = perturbation from averaged variable

I. Introduction

Boundary-layer transition (BLT) accounts for a major source of uncertainty in the heating loads on high-speed vehicles. Therefore, the prediction and control of transition onset and the associated variation in aerothermodynamic parameters in high-speed flows are critical factors in the design of next-generation aerospace vehicles. Although many practical high-speed vehicles are blunt, the mechanisms that lead to boundary layer instability and transition on blunt bodies are much less thoroughly understood at present compared to those on sharp bodies. Both experimental and numerical studies have established that laminar–turbulent transition in axisymmetric boundary layers over sharp cones at zero degrees angle of attack can be attributed to the modal growth of Mack's second mode instabilities [1]. For small values of nosetip bluntness, studies indicate that the transition location moves downstream with increasing nose radius, due to the formation of an entropy layer that stabilizes the amplification of Mack's second mode instabilities [2]. Thus, the observed delay in transition onset at small bluntness is consistent with the predictions of the linear, modal instability analysis. However, although such modal instability analysis predicts a continued delay in boundary-layer transition even at relatively large values of nose bluntness, experiments indicate that the downstream movement in transition actually slows down and eventually reverses when the nose bluntness exceeds a certain critical range of values [2–6].

Alternative theoretical paradigms based on nonmodal disturbance amplification have been proposed to explain the phenomenon of transition reversal. For instance, computations have identified planar [7–9] and oblique [8, 9] traveling disturbances that peak within the entropy layer of a blunt cone at zero degrees angle of attack, and furthermore, can sustain significant amounts of nonmodal amplification. Furthermore, Paredes et al. [10] demonstrated that, even though the linear nonmodal disturbances are primarily concentrated outside the boundary layer, their nonlinear interaction can generate stationary streaks that penetrate and amplify within the boundary layer, eventually inducing the onset of transition via the breakdown of these streaks. Therefore, their results suggest that the nonmodal amplification of nonstationary disturbances could play a role in the measured frustum transition for moderately blunt cones if they can be excited under a natural disturbance environment. However, the scope of these previous studies did not extend to addressing the origin of these nonmodal traveling disturbances that peak within the entropy layer. A follow-on study is therefore necessary to provide further information regarding the role of the freestream disturbances and the nonmodal growth of traveling disturbances within the entropy layer during the transition process. It is particularly important to establish a link between the measured transition in the absence of modal disturbance amplification and the freestream acoustic disturbances in a noisy wind-tunnel environment, given that almost all available experimental observations of the blunt cone transition phenomenon have been made in conventional (i.e., "noisy") hypersonic wind tunnels.

To date, most studies of boundary-layer receptivity in the hypersonic regime have been carried out using either a random inflow forcing across a broad range of frequencies and wavenumbers [11–13], or assumed incoming freestream disturbance fields with plane acoustic waves [14, 15]. For instance, Balakumar and Chou [15] studied simulations of hypersonic boundary-layer flows over a 7° half-angle straight cone with varying bluntness at a freestream Mach number of 10. In their study, an attempt was made to predict transition onset for flow over cones by using the measured freestream spectrum and two-dimensional numerical simulations. Only plane two-dimensional acoustic waves were imposed in the simulations, unlike the 3D noise field radiated from the nozzle walls that impinges on a test article at oblique angles. Although this approach provided encouraging results for a sharp cone under different flow conditions, the predictions for the flow over a medium blunt cone were not very satisfactory. Balakumar et al. [16] further examined the response of a Mach 3.5 flow over a sharp, 7° half-angle cone to oblique acoustic waves described by ad hoc analytical expressions. However, because the process of nonmodal amplification is intrinsically due to the interference of multiple eigenmodes of the underlying flow, it is unclear how well the simple form of freestream disturbances employed in that study would perform in predicting BLT over a blunt body.

In an unheated hypersonic wind tunnel with adequate flow conditioning, the freestream disturbance environment is dominated by acoustic radiation from tunnel-wall turbulent boundary layers (TBLs) (Figure 1) [17–22]. The effect of tunnel noise on BLT in conventional hypersonic wind tunnels has not been well characterized, largely due to the lack of an adequate knowledge base concerning the stochastic disturbance field associated with acoustic radiation from the turbulent boundary layers along the tunnel walls, making it difficult to relate the computational results to experimentally observed phenomena such as transition reversal over blunt cones from conventional hypersonic wind tunnels. Significant recent progress has been made in characterizing the acoustic disturbance field in hypersonic ground facilities via coordinated computations and experiments by the specialists group AVT-240 of NATO STO [23]. Specifically, the current authors conducted direct numerical simulations (DNS) of the stochastic noise radiation within hypersonic

Table 1 Preshock freestream conditions and wall temperature for DNS of a Mach 8 cone.

$M_{1,\infty}$	$U_{1,\infty}$(m/s)	$\rho_{1,\infty}$ (kg/m^3)	$T_{1,\infty}$ (K)	T_w (K)	T_w/T_r	$Re_u \times 10^6$ (1/m)
8.085	1091.9	0.0345	43.95	298	0.537	12.2

wind-tunnel facilities, elucidating the physics of noise generation inside the turbulent nozzle wall boundary layer and providing multipoint statistics to characterize the spatiotemporal structure of the freestream noise. The DNS-predicted noise spectra achieved encouraging agreement with those measured in experiments. These simulations have established the foundation for a "virtual" testing of the hypersonic BLT in a digital wind tunnel, and also provided the basis for the current work.

The objective of this paper is to numerically characterize the boundary-layer receptivity process of a Mach 8 blunt circular cone model to broadband freestream acoustic disturbances typical of a conventional hypersonic wind tunnel. The goal is to elucidate tunnel-noise effects within the transition reversal regime. To generate the "tunnel-like" freestream acoustic disturbances, a precursor DNS of acoustic radiation from turbulent nozzle-wall boundary layers has been conducted at the experimental conditions of the Sandia Mach 8 Hypersonic Wind Tunnel HWT-8 [24]. The broadband freestream disturbances radiated from the nozzle wall are then extracted and imposed at the outer boundary of the cone DNS. The induced instabilities over the cone model within the DNS are compared with the nonmodal analysis to provide further information regarding the role of the freestream disturbances, and the nonmodal growth of traveling disturbances within the entropy layer.

The paper is structured as follows. The flow conditions, numerical methods, and the methods for generating broadband "tunnel-like" acoustic disturbances are outlined in Section II. Section III presents DNS results of boundary-layer receptivity over a 7° half-angle blunt cone in comparison with stability analysis, including both two-dimensional axisymmetric DNS with linear planar acoustic waves and full-fledged three-dimensional DNS subject to broadband "tunnel-like" disturbances. A summary of the work is given in Section IV.

II. Flow Conditions and DNS Methodology

DNS of boundary-layer instability and transition are conducted over a 0.517-m-long, 7° half-angle cone with a blunt nose radius of 5.2 mm. To simulate BLT over the cone model within a digital wind tunnel, a precursor DNS of the full-scale axisymmetric nozzle of the Sandia HWT-8 was first conducted at a nominal operational condition of total pressure of $P_0 \approx 4692$ kPa and total temperature of $T_0 \approx 617$ K, and the flow conditions (including the unsteady acoustic disturbances) at the center of the nozzle near the nozzle exit were extracted and used for the primary cone simulation. More details of the precursor DNS of the digital wind tunnel along with the methodology for extracting freestream acoustic disturbances will be introduced in Section II.C. Table 1 summarizes the extracted mean freestream conditions used for the current cone DNS. The wall temperature of the cone is 298 K, corresponding to a wall-to-recovery temperature ratio of $T_w/T_r \approx 0.537$.

A. Governing Equations and Numerical Methods

To simulate boundary-layer instability and transition on a circular cone, the full three-dimensional compressible Navier-Stokes equations in conservation form were solved numerically in cylindrical coordinates. The working fluid was nitrogen (with an ideal gas constant of $R = 296.7$ J/(K·kg)) and fell within the perfect gas regime. The usual constitutive relations for a Newtonian fluid were used: the viscous stress tensor was linearly related to the rate-of-strain tensor, and the heat flux vector was linearly related to the temperature gradient through Fourier's law. The coefficient of viscosity μ was computed from Keyes law [25], and the coefficient of thermal conductivity κ was computed from $\kappa = \mu C_p/Pr$, with the molecular Prandtl number $Pr = 0.71$. The inviscid fluxes of the governing equations were computed using a seventh-order weighted essentially nonoscillatory (WENO) scheme [26]. The viscous fluxes were discretized using a fourth-order central difference scheme, and time integration was performed using a third-order low-storage Runge-Kutta scheme [27].

The singularity at the polar axis, as manifested in the $1/r$ terms of the governing equations, is handled by shifting the grid points in the radial direction by one half of the mesh spacing, following the approach proposed by Mohseni and Colonius [28]. In their approach, the use of less accurate one-sided finite difference schemes for the purpose of evaluating radial derivatives close to the pole ($r = 0$) is eliminated by mapping the flow domain from $(0, R) \times (0, 2\pi)$

to $(-R, R) \times (0, \pi)$, where R is the radius of the computational domain. The time step limitation due to the decrease in azimuthal spacing in the vicinity of the centerline (or pole) is addressed by dropping every few grid points (which amounts to increasing the grid spacing) in the azimuthal direction as $r \rightarrow 0$ in the computation of the azimuthal derivative [29].

The details of the DNS methodology have been documented in our previous simulations of acoustic radiation from turbulent boundary layers [30–35].

B. Simulation Setup and Boundary Conditions

To numerically investigate the transitional and turbulent boundary layer over a circular cone that is subject to "tunnel-like" freestream acoustic disturbances, the DNS is set up with the inflow boundary of the computational domain lying outside the leading-edge shock of the cone. "Tunnel-like" freestream acoustic disturbances are then introduced by prescribing flow variables at the inflow boundary based on the data saved from the precursor DNS of the disturbance environment inside a digital wind tunnel that pertains to an empty wind-tunnel configuration (i.e., without the test article). Fluctuation data within the freestream region of the precursor DNS is extracted and, after necessary reconstruction, fed through the inlet and the outer boundary of the computational domain of the DNS involving the cone (See Section II.C for details of the tunnel-noise extraction process). Given the time step limitation due to the requirement of a very fine grid near the nose of the cone, the cone DNS have been conducted in multiple stages involving three overlapping streamwise domains as schematically shown in Figure 1. The computation of Box 1 is done near the nose region, with a very small time step (referred to as Box1 DNS). For Box 2 and Box 3 simulations, wherein larger time steps can be used to evolve the boundary layer disturbances internalized within the upstream region, the inflow conditions are prescribed using the data saved from the upstream DNS box. A multidomain simulation approach of this type was previously applied to the DNS of BLT over a cone [36, 37]. On the wall, no-slip conditions are applied for the three velocity components, and an isothermal condition is used for the temperature. At the outlet boundaries, unsteady nonreflecting boundary conditions are imposed. Periodic boundary conditions are used in the azimuthal direction. The details of the grid dimensions, domain size, and resolutions of the cone DNS are listed in Table 2. The selection of grid parameters and other aspects of the numerical solution was based on extensive experience with a similar class of flows.

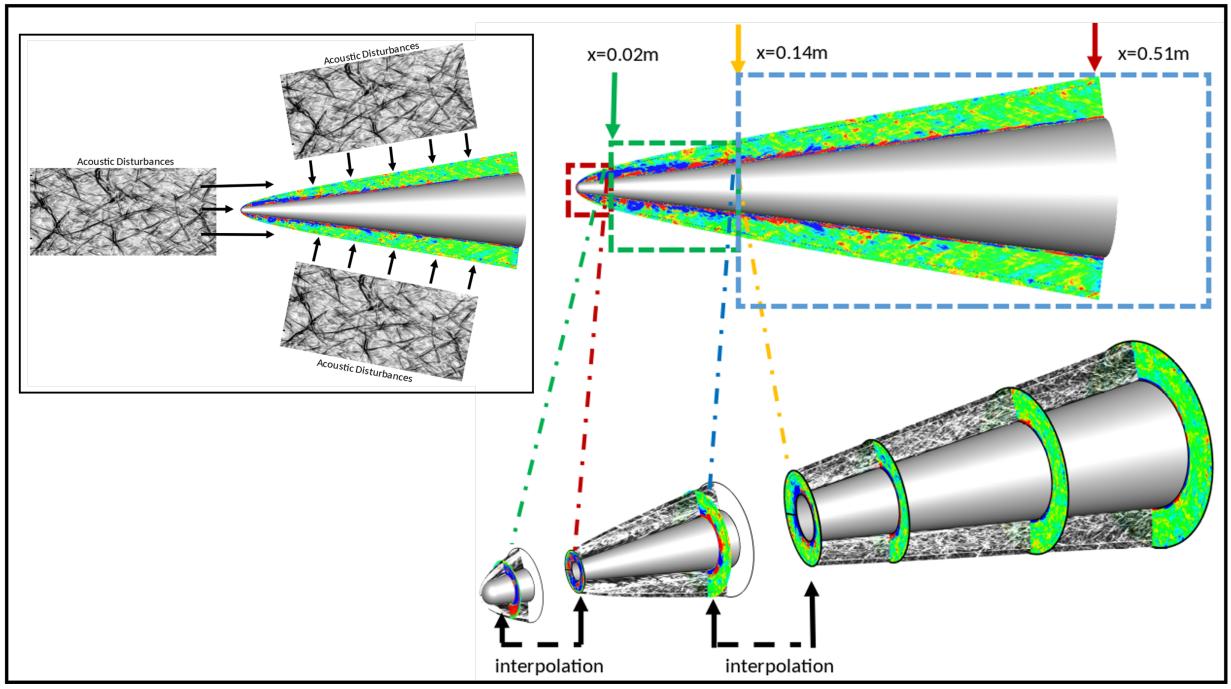

Fig. 1 Computational domain and simulation setup for DNS of Mach 8 flow over a blunt 7-deg half-angle circular cone with a blunt nose radius of $R_n = 5.2$ mm. The instantaneous flow is shown by the numerical schlieren (gray-scale) and temperature fluctuations (colored).

Table 2 Domain size and grid resolution for the cone DNS runs. $\mathbf{x_{range}}$ indicates the streamwise range of DNS boxes. N_x, N_θ and N_r are the grid points in the streamwise, azimuthal, and radial directions, respectively. Δx is the streamwise wall-paralleled grid spacing, $(r\Delta\theta)^+_w$ is the azimuthal grid spacing at the wall, and $\Delta z_{n,w}$ and $\Delta z_{n,e}$ are the wall-normal grid spacing at wall and boundary-layer edge, respectively. The leading edge of the cone corresponds to $x = -5.2$ mm, and the superscript "+" denotes normalization by the viscous length z_τ at $x = 0.3$ m for all the boxes.

Case	$N_x \times N_\theta \times N_r$	x (m)	Δx^+_{min}	Δx^+_{max}	$(r\Delta\theta)^+_w$	$\Delta z^+_{n,w}$	$\Delta z^+_{n,e}$
Box 1	$2800 \times 256 \times 1440$	-0.0061 - 0.02	0.23	0.23	3.82	0.11	0.16
Box 2	$1050 \times 1024 \times 1440$	0.01 - 0.14	0.23	4.72	3.13	0.26	0.39
Box 3	$2100 \times 1024 \times 1440$	0.13 - 0.51	4.72	4.72	6.22	0.37	0.55

C. "Tunnel-like" Acoustic Disturbance Generation and Extraction

1. DNS of Full-Scale Axisymmetric Nozzle of Sandia HWT-8

To generate the incident freestream acoustic disturbances for the targeted DNS of a cone, a precursor DNS of the full-scale axisymmetric nozzle of the Sandia HWT-8 was conducted with an emphasis on characterizing the properties of freestream acoustic disturbances in the test section of the tunnel. The simulated flow conditions fall within the range of tunnel operating conditions, and correspond to a total pressure of $P_0 = 4692$ kPa and a total temperature of $T_0 = 617$ K. Figure 2 shows the computational setup of the precursor simulation of the Sandia HWT-8 for generating the incident acoustic field. The tunnel configuration starts with the converging section upstream of the nozzle throat, which is located at $x \approx 0$ m. Note that we have used a coordinate system with $x = 0$ corresponding to the nozzle throat here, which is different from that in the cone simulations reported in Section III, where $x = 0$ corresponds approximately to the nose of the cone. The diverging section spans from $x \approx 0$ m to $x \approx 2.6$ m, followed by the test section. The DNS domain starts slightly downstream of the nozzle throat at $x = 0.07$ m with a local freestream Mach number of $M_\infty = 2.7$, and ends at the nozzle exit at $x = 2.6$ m with a freestream Mach number of $M_\infty \approx 8.0$. Additional details of the tunnel-noise simulation can be found in Duan et al. [35].

Figure 3 shows an instantaneous visualization of the density gradient associated with the radiated acoustic field in the Sandia HWT-8. The prominent structures associated with acoustic fluctuations within the freestream region exhibit a preferred orientation of $\theta \approx 20°$ with respect to the nozzle centerline within the streamwise-radial plane. The density gradients at a given axial location of the nozzle reveal the omnidirectional origin of the acoustic field, which adds to the stochastic nature of the wave front pattern. The spatiotemporal structures of these freestream acoustic fields is extracted and subsequently used to define the inflow and outer boundary conditions for the cone DNS.

2. Extraction and Reconstruction of Freestream Acoustic Disturbances

To model the acoustic field radiated from the turbulent nozzle-wall boundary layer of a hypersonic wind tunnel, we represent the acoustic perturbations in the free stream (i.e., outside of the turbulent boundary layer) as the superposition of a large number of plane wave components:

$$\begin{bmatrix} p'_{1,\infty} \\ \rho'_{1,\infty} \\ u'_{1,\infty} \\ v'_{1,\infty} \\ w'_{1,\infty} \\ T'_{1,\infty} \end{bmatrix} = \sum_{j=1}^{N} \begin{bmatrix} 1 \\ \frac{1}{\bar{c}^2_{1,\infty}} \\ \frac{1}{\bar{\rho}_{1,\infty}\bar{c}_{1,\infty}} \left(\frac{k_{x,j}}{\|\mathbf{k}_j\|} \right) \\ \frac{1}{\bar{\rho}_{1,\infty}\bar{c}_{1,\infty}} \left(\frac{k_{y,j}}{\|\mathbf{k}_j\|} \right) \\ \frac{1}{\bar{\rho}_{1,\infty}\bar{c}_{1,\infty}} \left(\frac{k_{z,j}}{\|\mathbf{k}_j\|} \right) \\ \frac{(\gamma-1)\overline{T}_{1,\infty}}{\gamma \overline{p}_{1,\infty}} \end{bmatrix} \hat{p}_j(\mathbf{k}_j, \omega_j) e^{i(\mathbf{k}_j \cdot \mathbf{x} - \omega_j t + \phi_j)} + c.c. \tag{1}$$

Here, $\mathbf{x} = (x, y, z)$ denotes the vector of Cartesian spatial coordinates, $(\cdot)'_{1,\infty}$ denotes the perturbations with respect to the mean freestream quantities, and "$c.c.$" stands for complex conjugate. The quantities $\mathbf{k}_j = (k_{x,j}, k_{y,j}, k_{z,j})$, ω_j,

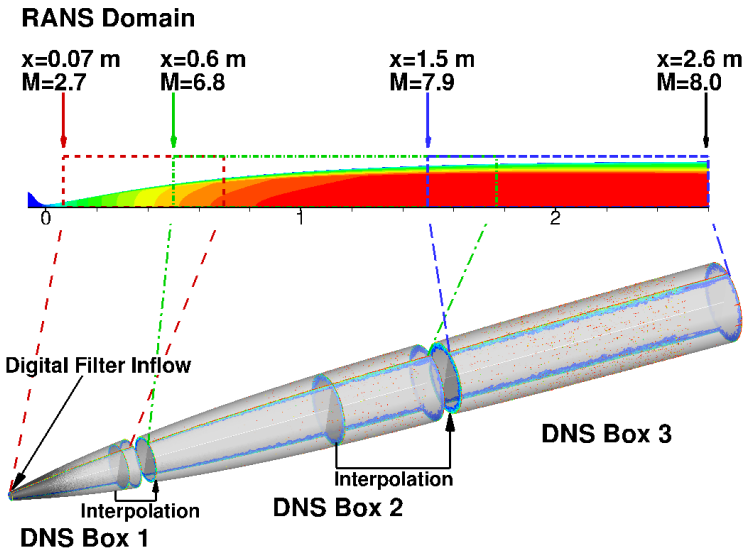

Fig. 2 Computational domain set up for the precursor DNS of the full-scale axisymmetric nozzle of Sandia HWT-8 [35].

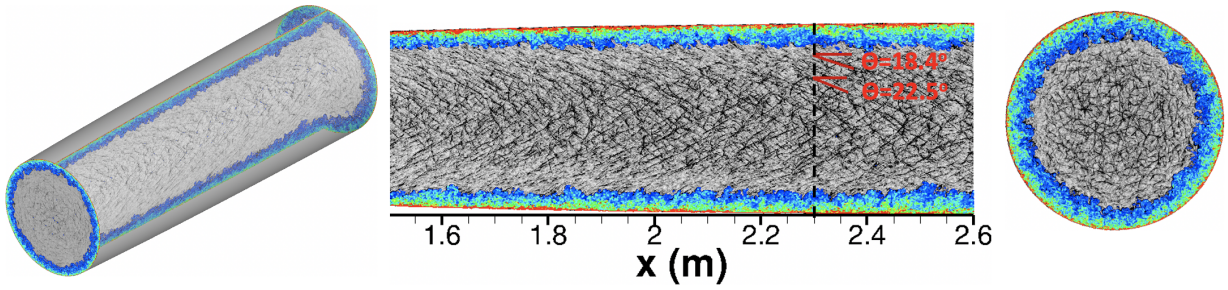

Fig. 3 Numerical schlieren images (i.e., density gradient contours) of radiated acoustic waves within the nozzle of the Sandia HWT-8 [35]. The vertical dashed line indicates the axial location of the selected cross section visualized in the right panel.

$\hat{p}_j$, and ϕ_j represent the wavenumber vector, angular frequency, complex amplitude, and phase, respectively, of the plane acoustic wave with index j. The norm of the wavenumber vector is defined as $\|\mathbf{k}_j\| \equiv \sqrt{k_{x,j}^2 + k_{y,j}^2 + k_{z,j}^2}$. The angular frequency ω_j of the jth wave is related to its wavenumber $\mathbf{k}_j$ via the dispersion relation for acoustic waves [38]:

$$\omega_j(\mathbf{k}_j) = \overline{\mathbf{u}}_{1,\infty} \cdot \mathbf{k}_j \pm \overline{c}_{1,\infty} \|\mathbf{k}_j.\|, \tag{2}$$

The corresponding group velocity $\overline{\mathbf{v}}_j$ of the acoustic waves can be written as:

$$\overline{\mathbf{v}}_{\pm,j} \equiv \frac{\partial \omega_j}{\partial \mathbf{k}_j} = \overline{\mathbf{u}}_{1,\infty} \pm \overline{c}_{1,\infty} \left(\frac{\mathbf{k}_j}{\|\mathbf{k}_j\|} \right). \tag{3}$$

The plus-minus sign (±) in Eq. (3) indicates that the group velocity of the acoustic waves can be faster or slower than the mean flow velocity, with the relative magnitude (with respect to the mean flow) equal to the speed of sound $\overline{c}_{1,\infty}$ along the wave front orientation $\mathbf{k}_j/\|\mathbf{k}_j\|$. Here, we follow the definition of McKenzie and Westphal [38] by referring to acoustic waves with $\overline{\mathbf{v}}_{+,j} = \overline{\mathbf{u}}_{1,\infty} + \overline{c}_{1,\infty} \left(\frac{\mathbf{k}_j}{\|\mathbf{k}_j\|} \right)$ as the "fast" acoustic waves and those with a group speed of $\overline{\mathbf{v}}_{-,j} = \overline{\mathbf{u}}_{1,\infty} - \overline{c}_{1,\infty} \left(\frac{\mathbf{k}_j}{\|\mathbf{k}_j\|} \right)$ as "slow" acoustic waves.

Given a tunnel operating condition with known time-averaged freestream quantities, the information required to complete the specification of the acoustic field according to the plane-wave model in Eq. (1) corresponds to the parameters $\mathbf{k}_j$, $\hat{p}_j$, ϕ_j and making a choice between fast and slow waves or a mixture thereof.

To determine the unknown parameters in Eq. 1 that are required to synthesize the broadband field of three-dimensional acoustic disturbances in the free stream region from the tunnel DNS as visualized in Figure 3, we first extract the instantaneous pressure field within a rectangular domain from the freestream region of the precursor DNS. The crossplane extent of this rectangular domain is chosen to be larger than the base radius of the cone model and the axial extent of the domain corresponds to the region from $x = 1.82$ m to $x = 2.23$ m, which is immediately upstream of where the cone is mounted within the tunnel. The size of the rectangular domain relative to the nozzle boundary layer thickness is approximately $(L_x/\delta_{nozzle}, L_y/\delta_{nozzle}, L_z/\delta_{nozzle}) = (10.1, 4.6, 4.6)$ and includes a total of $(1200, 400, 400)$ points in the axial and the two transverse directions, respectively, from the precursor DNS (Figure 4). Here, $\delta_{nozzle} = 38.5$ mm represents the nozzle-wall boundary layer thickness at $x = 2.1$ m, which denotes the axial midpoint of the acoustic domain. The selected domain for acoustic wave extraction is large enough to accommodate the largest freestream acoustic structures. After a detrending process to compute the acoustic pressure fluctuations $p'_{1,\infty}$ by subtracting the mean pressure $\overline{p}_{1,\infty}$, spatial fast Fourier transforms (FFT) are performed along each spatial direction of the rectangular domain. This provides the specification of the modal content of the acoustic fluctuations, including the wavenumber vector $\mathbf{k}_j = (k_{x,j}, k_{y,j}, k_{z,j})$, complex amplitude $\hat{p}_j$, and the phase angle ϕ_j for each individual mode j. Given the wavenumber vector $\mathbf{k}_j$ of each mode j, its frequency can be computed by Eq. 2 with the assumption of a slow acoustic wave. The dominance of slow acoustic waves (with a propagation speed slower than the sound speed) in the free stream of conventional supersonic and hypersonic tunnels has been suggested in multiple previous studies [23, 30, 31, 39], and will be further confirmed in Section II.C.3 for the current tunnel conditions. To guarantee that only statistically relevant modes are kept in the synthesized acoustic field, the three-dimensional spatial fast Fourier transform (FFT) is repeated within the same rectangular domain for a total of $N_f = 70$ snapshots of the instantaneous freestream acoustic fields, and the modal amplitudes $\hat{p}_j$ in the acoustic model from Eq. 1 are computed by using an average of the power spectral densities across the snapshots. However, to preserve the stochasticity of the reconstructed field, the phase angles (ϕ_j) in the acoustic model are derived from a single instantaneous snapshot of the extracted three-dimensional acoustic field. Additionally, because the WENO scheme used for the tunnel DNS requires at least 8 points per wavelength to accurately propagate a linear wave over multiple wavelengths, a low-pass wavenumber filter with spectral cut-off is applied to remove the small-wavelength waves that cannot be accurately resolved by the precursor DNS. To be conservative, we have also excluded any acoustic wave components that have frequencies higher than 1 MHz, which cannot be resolved with the given mesh resolution of the precursor DNS. The total number of plane waves included in the acoustic-wave ansats is $N \approx 375000$. Lastly, the acoustic disturbances generated according to the model in Eq. 1 are interpolated from the Cartesian domain used for spatial FFTs into a cylindrical domain and imposed at the outer boundary of the domain used for the three-dimensional DNS focused on the disturbance amplification and transition over a cone model (Section III.C).

It may be noted that the extraction of the acoustic modes was performed in the Cartesian domain and the results were interpolated into the cylindrical domain used for the DNS involving the cone. This allows us to use the computationally efficient FFT libraries to speed up the mode extraction process rather than dealing with the more expensive Hankel transformations required for the cylindrical coordinate system. It would also allow us to more easily extend the tunnel-noise generation technique to hypersonic wind tunnels with a rectangular/square nozzle shape such as NASA's 20 Inch Mach 6 Wind Tunnel [40].

3. Assessment of Acoustic Disturbance Model

Figure 5 shows the power spectral density (PSD) of freestream acoustic disturbances based on the acoustic model from Eq. 1 after calibration against the data from the precursor DNS. Very good agreement is achieved between the acoustic model with the slow-acoustic-wave assumption and the DNS data, reconfirming the dominance of slow acoustic waves in the radiated noise from the nozzle-wall turbulent boundary layer.

Figure 6 shows both wavenumber spectra and frequency spectra of the freestream acoustic disturbances based on the calibrated acoustic model from Eq. 1. The results plotted herein allow a comparison of the spectral estimates based on acoustic extraction with multiple spatial domains with those obtained from the precursor DNS of an empty tunnel. Here, the rectangular domain sizes as described in Section II.C.2 are measured in terms of the local nozzle boundary-layer thickness δ_{nozzle} at $x \simeq 2.1$ m (i.e., 2.1 meters downstream of the nozzle throat), and the wavenumber and frequency spectra of both pressure and streamwise velocity fluctuations are included

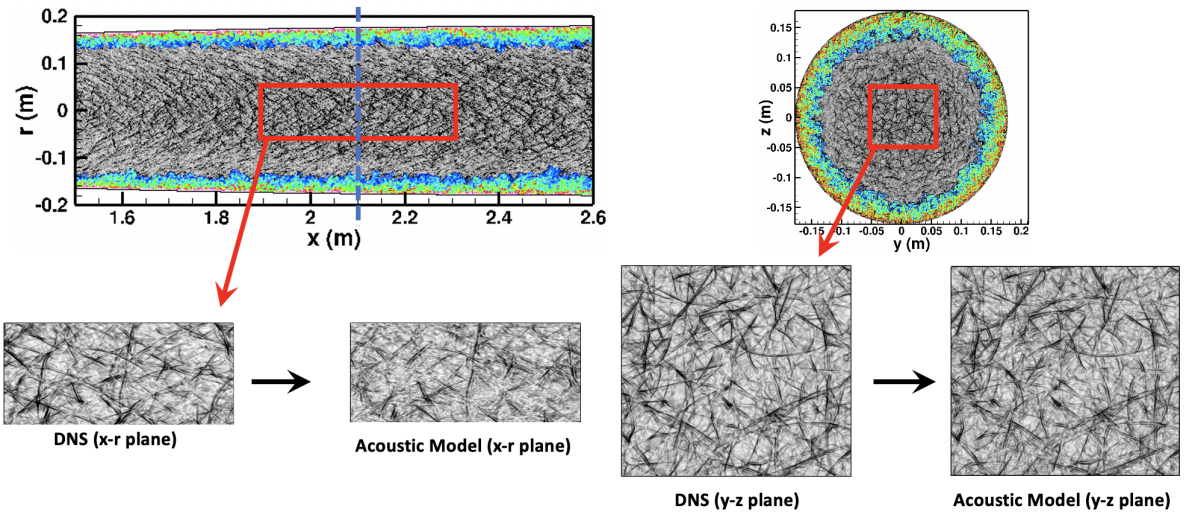

Fig. 4 Schematic of the rectangular domain for extracting freestream acoustic disturbances from the precursor DNS of empty wind tunnel. The vertical dashed line indicates the streamwise location of the selected cross-plane visualized on the top right.

to show the sensitivity of different acoustic quantities to the model parameters. With the selected domain size of $(L_x/\delta_{nozzle}, L_y/\delta_{nozzle}, L_z/\delta_{nozzle}) = (10.1, 4.6, 4.6)$ for extracting the freestream acoustic waves, excellent comparisons between the model and the DNS are achieved in spectra of both pressure and velocity fluctuations. A further comparison among model predictions with different domain sizes suggests that the model-predicted frequency spectrum is insensitive to the longitudinal and transverse extents of the domain, while a large enough domain size in the transverse directions is indeed required for the model-predicted wavenumber spectra to match with the tunnel DNS.

Figure 7 depicts visualizations from the temporal evolution of freestream acoustic disturbances in a cross plane (i.e., y-z plane). Results are shown both for the acoustic field predicted by the model from Eq. 1 and its comparison with the corresponding snapshots from the precursor tunnel DNS. Here, the freestream acoustic disturbances are visualized by the numerical schlieren (i.e., density gradient contours). The visualization at $t = 0$ corresponds to the snapshot from which the modal phase ϕ_j of all the plane waves in the ansats are derived, and the time delay is measured in terms of the integral time scale Λ of the freestream pressure disturbances. The apparent similarity in the instantaneous acoustic structures between the model and DNS confirms that the freestream acoustic disturbances generated from the acoustic model closely mimic those of the DNS over time intervals of at least $t = 9\Lambda$ (which corresponds to at least 1.5 times of the large-eddy turnover time $\delta_{nozzle}/U_{1,\infty}$ of the nozzle-wall boundary layer), while preserving the stochastic nature of the freestream acoustic field.

III. Results

In this section, results from the stability analysis and DNS for the boundary layer over a Mach 8 cone are reported. First, the findings from both modal and nonmodal instability analyses at the selected Mach 8 conditions are presented for sharp and blunt cones, respectively. Next, as a precursor validation of the DNS approach, DNS of axisymmetric disturbances in the boundary layer flows over the sharp and blunt cones are conducted for planar freestream acoustic disturbances, and the computed evolution of the instability waves excited by the freestream acoustic forcing are compared with those from the stability analysis. Finally, the results of a full-fledged three-dimensional DNS are presented for a blunt cone with tunnel acoustic disturbances.

A. Modal and Nonmodal instability analysis

In this section, we present the modal instability characteristics of the 7° half-angle cone at Mach 8 with nose radii equal to 0.05 mm and 5.2 mm. The nonmodal analysis of the blunter cone is also documented. Following the work of Refs. [8, 9], we use the harmonic linearized Navier Stokes equations (HLNSE), the reduced form of the HLNSE

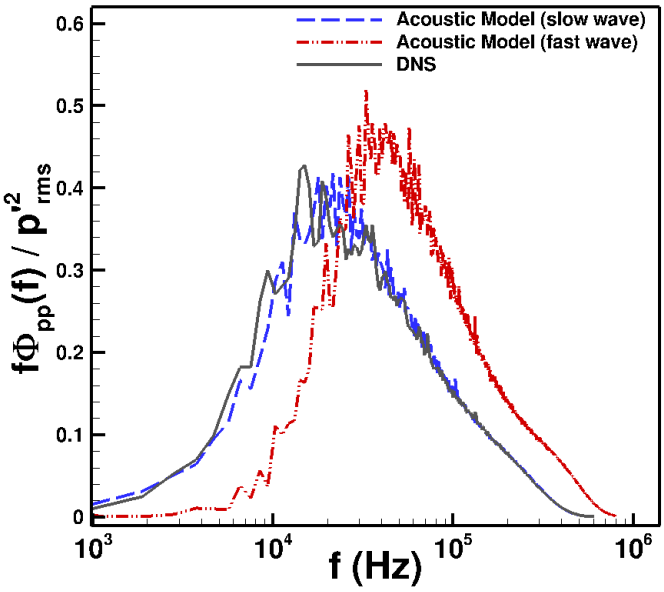

Fig. 5 PSD of freestream acoustic disturbances computed based on the calibrated acoustic model of Eq. 1 with fast (+) or slow (-) acoustic wave assumptions in comparison with that of the precursor tunnel DNS at $x \approx 2.1$ m).

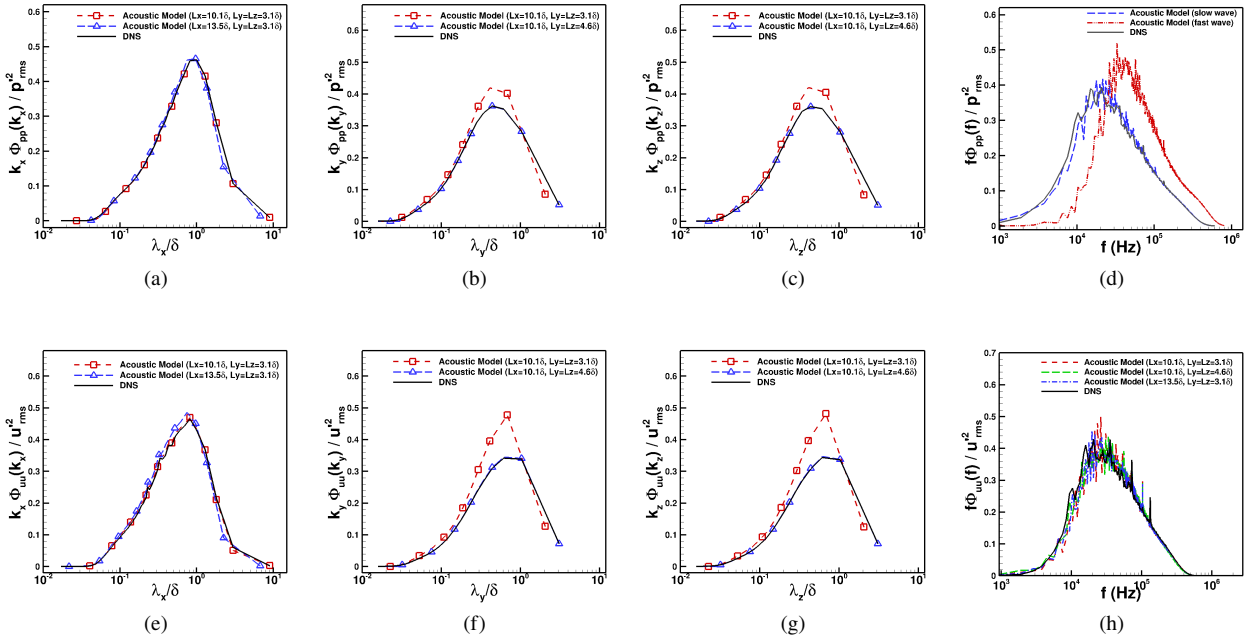

Fig. 6 Wavenumber spectra and frequency spectra of freestream acoustic disturbances computed based on the calibrated acoustic model of Eq. 1 with different spatial domain sizes in comparison with those of the precursor tunnel DNS. (a-d) pressure and (e-h) streamwise velocity. The domain size for extracting freestream acoustic is normalized by local nozzle boundary-layer thickness of $\delta = 38.5$ mm at $x \approx 2.1$ m).

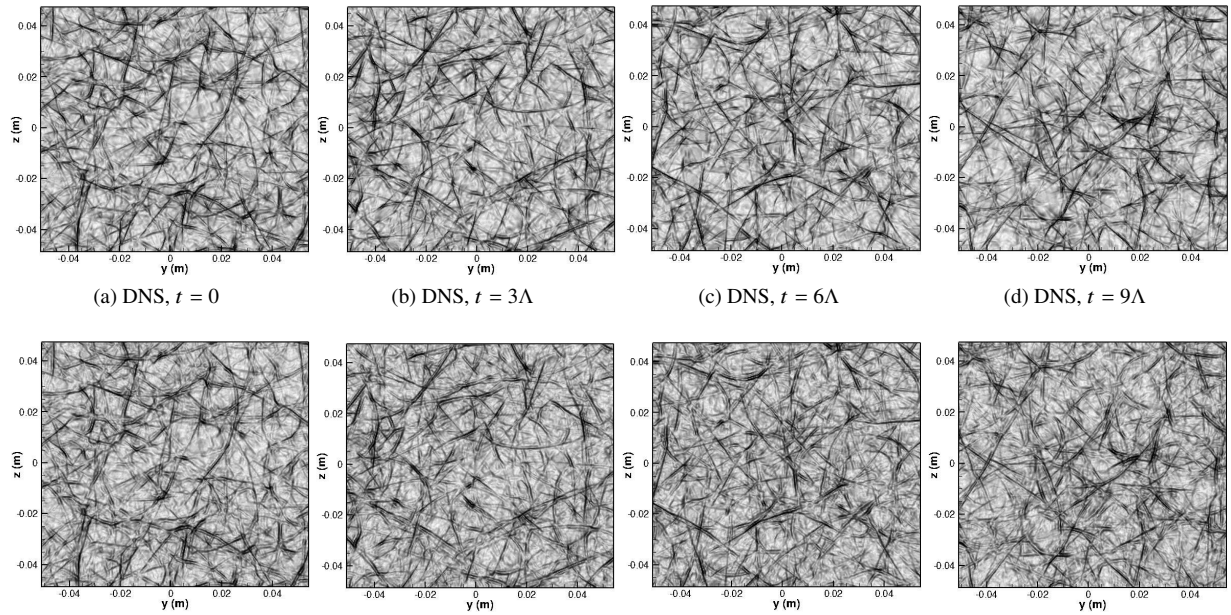

(a) DNS, $t = 0$ (b) DNS, $t = 3\Lambda$ (c) DNS, $t = 6\Lambda$ (d) DNS, $t = 9\Lambda$

(e) Model, $t = 0$ (f) Model, $t = 3\Lambda$ (g) Model, $t = 6\Lambda$ (h) Model, $t = 9\Lambda$

Fig. 7 Temporal evolution of freestream acoustic disturbances in a cross-plane (y-z plane) generated by the calibrated acoustic model of Eq. 1 in comparison with those from the precursor tunnel DNS. Here, the freestream acoustic disturbance field is visualized via numerical schlieren (i.e., density gradient contours) and the time delay is measured in terms of the integral time scale $\Lambda = 5.8$ μs of the freestream acoustic disturbances.

(RHLNSE), and the linear parabolized stability equations (PSE) frameworks to investigate both modal and nonmodal disturbances.

For this problem, the computational coordinates are defined as an orthogonal, body-fitted coordinate system, with (ξ, η, ζ) denoting the streamwise, wall-normal, and azimuthal coordinates, respectively, and (u, v, w) representing the corresponding velocity components. Density and temperature are denoted by ρ and T, respectively. The metric factors are defined as

$$h_\xi = 1 + \kappa\eta, \tag{4}$$

$$h_\zeta = r_b + \eta\cos(\theta), \tag{5}$$

where h_ξ and h_ζ are associated with the streamwise and azimuthal curvature, respectively, κ denotes the streamwise curvature, r_b is the local radius, and θ is the local half-angle along the axisymmetric surface, i.e., $\sin(\theta) = dr_b/d\xi$. The Cartesian coordinates are represented by (x, y, z). The vector of perturbation variables is denoted by $\tilde{\mathbf{q}}(\xi, \eta, \zeta, t) = (\tilde{\rho}, \tilde{u}, \tilde{v}, \tilde{w}, \tilde{T})^T$, and the vector of disturbance functions is $\breve{\mathbf{q}}(\xi, \eta, \zeta) = (\breve{\rho}, \breve{u}, \breve{v}, \breve{w}, \breve{T})^T$. The vector of basic state variables is $\bar{\mathbf{q}}(\xi, \eta, \zeta) = (\bar{\rho}, \bar{u}, \bar{v}, \bar{w}, \bar{T})^T$. For axisymmetric geometries at zero degrees angle of attack, the basic state variables are independent of the azimuthal coordinate, and the linear perturbations can be assumed to be harmonic in time and azimuthal direction, which lead to the following expression for the perturbations,

$$\tilde{\mathbf{q}}(\xi, \eta, \zeta, t) = \breve{\mathbf{q}}(\xi, \eta)\exp\left[\mathrm{i}\,(m\zeta - \omega t)\right] + \text{c.c.}, \tag{6}$$

where the m is the azimuthal wavenumber and ω is the angular frequency.

The PSE are used to study the amplification of the boundary-layer instability waves. The PSE approximation to the HLNSE is based on isolating the rapid phase variations in the streamwise direction via the disturbance ansatz

$$\breve{\mathbf{q}}(\xi, \eta) = \hat{\mathbf{q}}(\xi, \eta)\exp\left[\mathrm{i}\int_{\xi_0}^{\xi}\alpha(\xi')\,\mathrm{d}\xi'\right], \tag{7}$$

where the amplitude functions $\hat{\mathbf{q}}(\xi, \eta, \zeta) = (\hat{\rho}, \hat{u}, \hat{v}, \hat{w}, \hat{T})^T$ vary slowly in the streamwise direction in comparison with the phase term. The onset of laminar-turbulent transition is estimated using the logarithmic amplification ratio, the

so-called N-factor, relative to the lower bound location ξ_I where the disturbance first becomes unstable,

$$N_E = -\int_{\xi_I}^{\xi} \alpha_i(\xi')\,\mathrm{d}\xi' + 1/2 \ln\left[\hat{E}(\xi)/\hat{E}(\xi_I)\right], \tag{8}$$

where $\hat{E}$ denotes the energy norm of $\hat{\mathbf{q}}$ as defined by Chu [41].

Figures 8a and 8b show the N-factor of planar second Mack mode waves ($m = 0$) for the selected sharp ($R_n = 0.05$ mm) and blunt ($R_n = 5.2$ mm) 7° half-angle cones at the freestream conditions listed in Table 1. The experiments of Casper et al. [42] with the sharp cone at the present conditions measured a transition location around $\xi = 0.25$ m. The corresponding N-factor at the transition location is $N_{E,tr} = 7.5$. However, the amplification of Mack mode waves is drastically reduced by the blunt nose tip. The first neutral location is delayed up to $\xi = 0.4$ m and the N-factor values along the cone length are below $N_E = 1.5$, which is deemed too low to lead to transition onset via purely modal amplification.

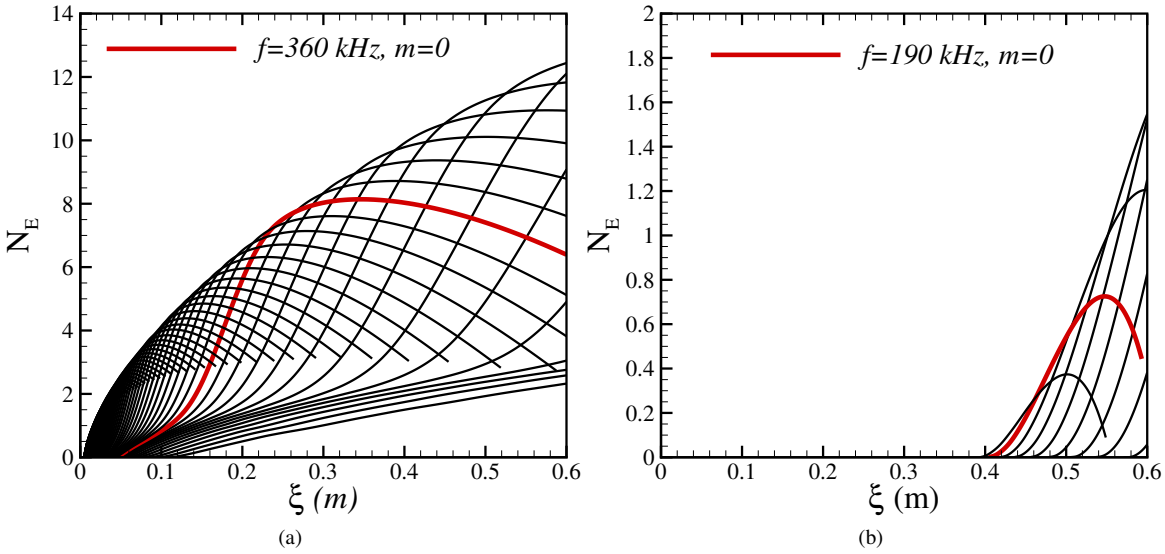

Fig. 8 N-factor curves of planar disturbances over the (a) $r_n = 0.05$ **mm cone with frequency increments of** 20 **kHz and the (b)** $r_n = 5.2$ **mm cone with frequency increments of** 5 **kHz.**

The nonmodal instability analysis is conducted with the RHLNSE. The optimal initial disturbance, $\tilde{\mathbf{q}}_0$, is defined as the initial (i.e., inflow) condition at ξ_0 that maximizes the objective function, J, which is defined as a measure of disturbance growth over a specified interval $[\xi_0, \xi_1]$. The definition used in the present study corresponds to the mean energy gain $J = G_{E,mean}$, which is defined as

$$G_{E,mean} = \frac{1}{\xi_1 - \xi_0} \frac{\int_{\xi_0}^{\xi_1} E(\xi')\, d\xi'}{E(\xi_0)}. \tag{9}$$

The variational formulation of the problem to determine the maximum of the objective functional J leads to an optimality system [43], which is solved in an iterative manner, starting from a random solution at ξ_0 that must satisfy the boundary conditions.

Figure 9 shows the nonmodal amplification of stationary and traveling, planar and oblique disturbances for the blunt cone with $R_n = 5.2$ mm. The inflow and outflow optimization locations are selected at $\xi_0 = 0.064$ m and $\xi_1 = 0.5$ m, respectively. Similar to the findings of Paredes et al. [9] for blunt cones at Mach 6, the maximum energy gain is achieved by a stationary ($f = 0$ kHz), three-dimensional perturbation. This stationary disturbance corresponds to the three-dimensional streaks studied by Paredes et al. [8]. Additionally, there is a peak in the energy gain contours for axisymmetric disturbances ($m = 0$), with an associated frequency of $f = 175$ kHz. The energy amplification of traveling oblique disturbances is comparable to the peak amplification of axisymmetric waves. As shown by Paredes et al. [9], these axisymmetric and oblique traveling disturbances are initially tilted against the flow direction and increase in

magnitude while rotating downstream. The energy amplification is mainly attributed to the temperature perturbation within the entropy layer, where also exhibits a gradient in the mean flow temperature.

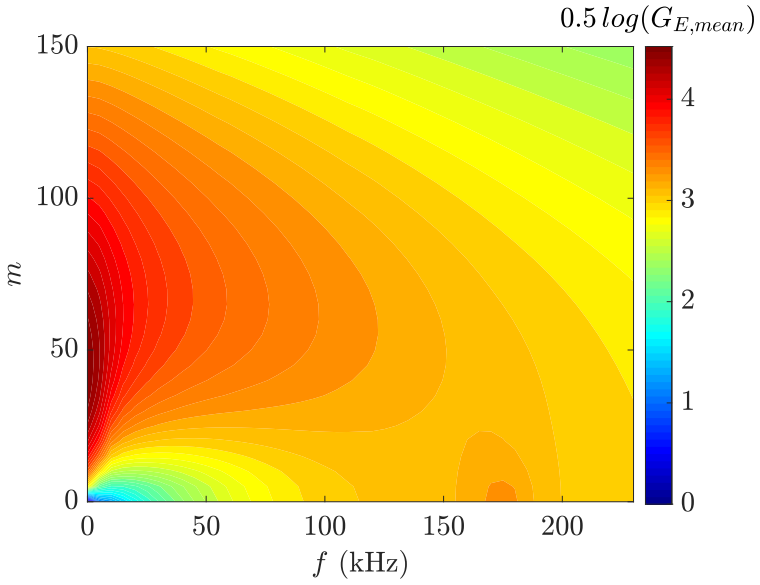

Fig. 9 Contors of $0.5\log(G_{E,mean})$ in the (m, f) plane of laminar boundary-layer flow along the blunt cone with $r_n = 5.2$ mm. The inflow and outflow optimization locations are selected at $\xi_0 = 0.064$ m and $\xi_1 = 0.5$ m.

B. Two-Dimensional Axisymmetric DNS

In this section, results of the DNS involving axisymmetric disturbances at selected frequencies are reported for both sharp and blunt cones at Mach 8. In each DNS, planar and slow acoustic waves with an amplitude of $A_p = 3.2\times10^{-4}\, p_{1,\infty}$ and frequencies ranging from 50 kHz to 500 kHz (with an increment of 50 kHz) are imposed at the outer boundary of the DNS domain. The boundary layer instabilities excited by the freestream forcing are compared with those from the stability analysis. A similar axisymmetric calculation was conducted by Balakumar et al. [16] for a straight cone with 7 deg half-angle and several values of the nose bluntness parameter for a freestream Mach number of 10.

Figure 10 shows the N factors based on wall-pressure fluctuations as computed via the DNS and the linear PSE, respectively, for two small nose radii of $R_n = 0.05$ mm and $R_n = 0.5$ mm. Given that the instability over a sharp cone is dominated by Mack's second mode waves that are acoustic in nature, they can be well captured by the wall-pressure signal. For both nose radii, the generation of the instability waves inside the boundary layer and their subsequent exponential growth are captured within the DNS. The changes in the stability characteristics due to the variation of nose radii from $R_n = 0.05$ mm to $R_n = 0.5$ mm are small as the disturbances over both cones indicate similar growth factors relative to the leading edge region and reach similar N-factor values near the middle of the cone. For both cases, the N factors based on the DNS are in excellent agreement with those predicted by the modal analysis based on PSE.

Comparisons between the laminar basic states computed by the WENO based DNS code and the second-order finite-volume VULCAN flow solver by NASA [44] are presented in Figure 11 for the blunt cone with $R_n = 5.2$ mm. Results are presented for the density contours as well as boundary-layer profiles for selected flow variables. Similar to the sharp cone results, an excellent agreement is obtained between the current DNS results and those from VULCAN. With the base flow solutions cross validated, Figure 12 shows the instantaneous contours of temperature fluctuation due to the freestream acoustic disturbance at $f = 150$ kHz within the DNS, along with the results based on the nonmodal, optimal growth analysis for the same frequency. The strong similarities in term of wall-normal location and streamwise wavelength indicate that disturbances similar to those predicted by the optimal growth analysis may be excited by the freestream acoustic wave.

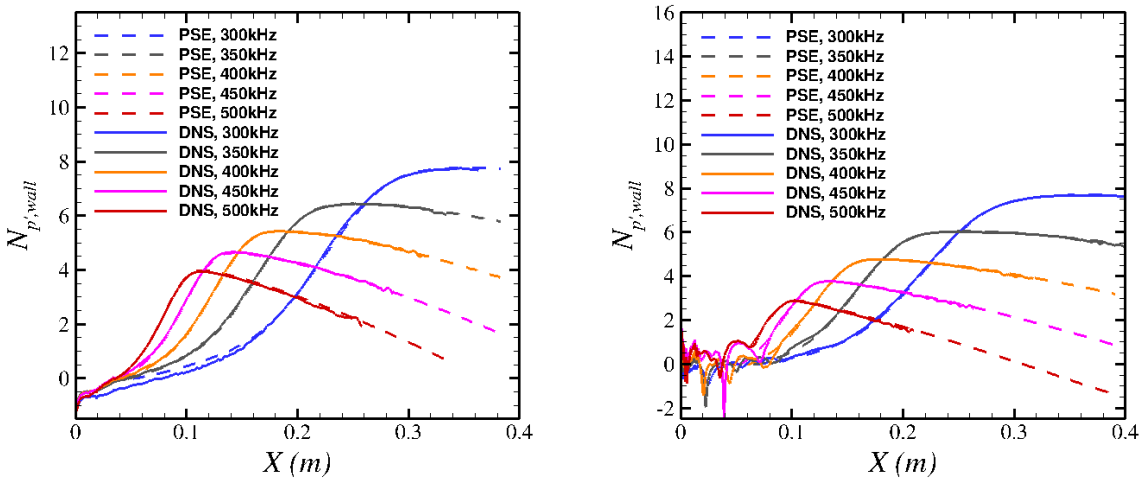

(a) R_n = 0.05 mm

(b) R_n = 0.5 mm

Fig. 10 N-factor curves of the wall pressure predicted by two-dimensional axisymmetric DNS of Mach 8 cones of R_n = 0.05 mm and 0.5 mm in comparison with those from the modal PSE analysis. In the DNS, 10 slow planar acoustic waves are imposed in the free stream with frequency increments of 50 kHz from 50 kHz to 500 kHz. Solid lines; DNS; Dashed lines: PSE.

C. Three-Dimensional DNS of blunt cone with tunnel-like acoustic disturbances

The results of the three-dimensional DNS of a Mach 8 blunt cone with $R_n = 5.2$ mm are presented next. Results are limited to an axial region of up to $x \simeq 0.45$ m because the duration of the simulation was insufficient to ensure statistical convergence until the end of the cone. For reference, the leading edge of the cone corresponds to $x = -5.2$ mm. As explained in subsection II.B, the reconstructed, tunnel-like freestream acoustic disturbances described in subsection II.C are used as the inflow forcing along the freestream boundary of the computational grid upstream of the bow shock. The full azimuthal domain of 2π radians is included in the DNS. Table 3 lists the boundary layer properties at a reference location of $x = 0.3$ m over the frustum of the blunt cone.

The evolution of the mean skin-friction coefficient $C_f = \tau_w/(0.5\rho_{2,\infty}U_{2,\infty}^2)$ and mean Stanton number $C_h = q_w/(\rho_{2,\infty}U_{2,\infty}C_p(T_r - T_w))$ based on the time average of the unsteady solution over a time interval of 0.08 ms is shown in Figure 13. The modeled freestream acoustic disturbances lead to Stanton number values that are approximately 10% higher within the nosetip region. However, the Stanton numbers for the acoustic forcing case recover to the laminar baseflow values for $x > 0.15$ m. A significant increase in the Stanton number values adjacent to the stagnation point (in comparison to the Stanton numbers for the laminar baseflow) has also been reported during wind tunnel tests in noisy wind tunnels [45]. On the other hand, the skin-friction coefficient C_f remains nearly identical to the baseflow values along the entire length of the cone, which indicates that the boundary layer remains laminar throughout the axial domain shown in the figure. Although the boundary layer remains laminar, the fluctuating wall quantities over the cone surface exhibit appreciable amplitudes relative to their mean value. For example, the fluctuations in surface pressure correspond to approximately two percent of the local mean values, whereas even larger relative fluctuation levels are seen in the surface shear stress and the heat flux.

Next, the spectral amplitude of the wall-pressure fluctuations are examined in the frequency and azimuthal wavenumber plane in Figure 14. The computed data at selected axial stations are Fourier transformed in both time and the azimuthal coordinate. The highest values of spectral density are generally confined to the low frequency range of up to approximately 50 kHz that also account for a major fraction of the signal energy in the tunnel-like freestream acoustic disturbances as shown in the premultiplied frequency spectra in Figure 5. However, in the aft part of the cone, one also observes the emergence of a secondary peak at higher frequencies in the range of 150 kHz to 200 kHz and azimuthal wavenumbers lower than approximately 20. Recall that the optimal growth analysis had also predicted a similar peak in the amplification factors in the same range of frequencies and for small values of m. Furthermore, computations for a Mach 6 blunt cone [9] had shown that only nonmodal disturbances with low azimuthal wavenumbers tend to penetrate

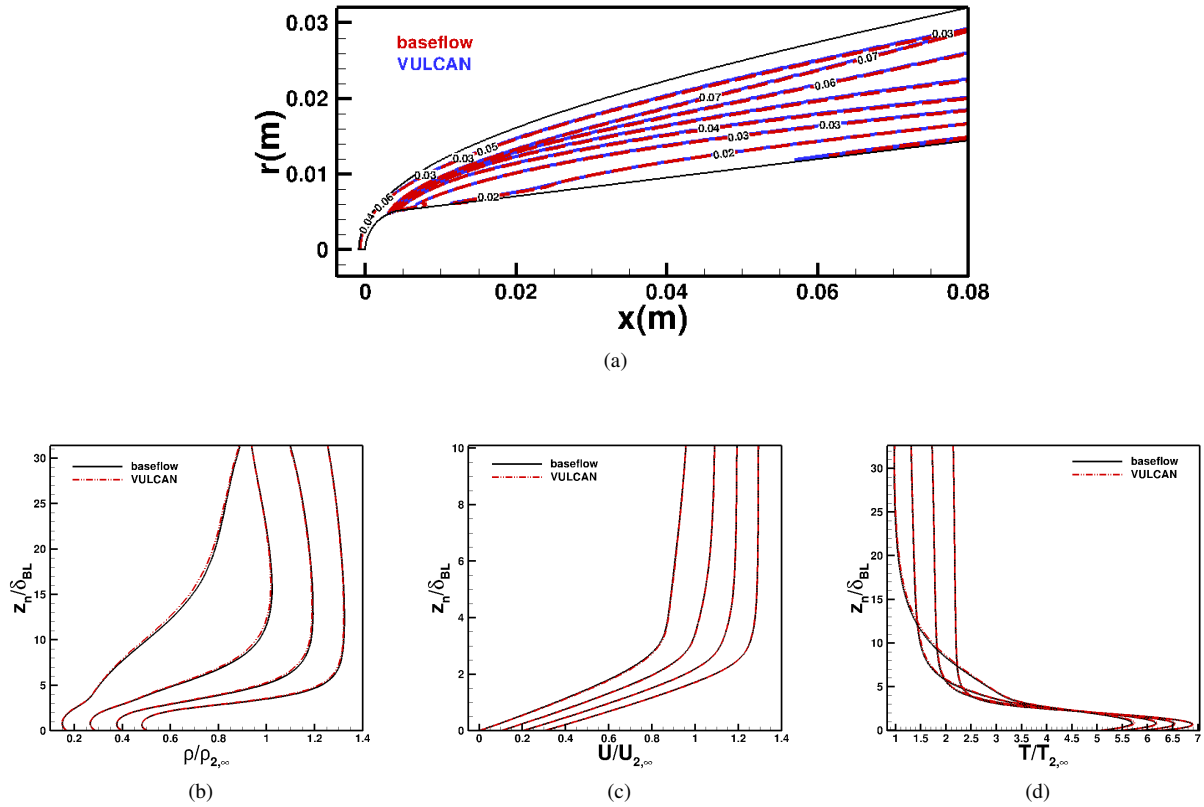

Fig. 11 Laminar base flow solutions for the blunt Mach 8 cone with $R_n = 5.2$ mm: comparison between the solutions based on the DNS code and NASA's VULCAN flow solver. In (b), (c), and (d), the wall-normal profiles are taken at $x = 0.1$, 0.2, 0.3, and 0.4 m, and the wall-normal distance z_n is normalized by the Blasius length scale is $\delta_{BL} = \sqrt{\nu_w x/U_{2,\infty}}$. The density, velocity, and temperature profiles are offset by 0.00631 kg/m^3, 107.4 m/s, and 24.564 K, respectively, from the last.

Table 3 Boundary layer properties at a reference location of $x = 0.3$ m over the cone frustum predicted by three-dimensional DNS with tunnel-like acoustic input. $(\cdot)_{2,\infty}$ denotes quantities behind the shock but outside the boundary layer (at $z_n/\delta \approx 4.75$).

x	$M_{2,\infty}$	$U_{2,\infty}$	$\rho_{2,\infty}$	$T_{2,\infty}$	Re_θ	Re_τ	Re_{δ_2}	θ	δ^*	δ	z_τ	u_τ	τ_w
(m)		(m/s)	(kg/m^3)	(K)				(mm)	(mm)	(mm)	(μm)	(m/s)	(Pa)
0.3	6.90	1077	0.0647	58.67	1157	40.3	327	0.103	2.17	1.67	41.5	32.9	14.1

M_e	U_e (m/s)	ρ_e (kg/m^3)	T_e (K)
3.73	967	0.0240	164.18

the boundary layer flow. Therefore, the wall-pressure signature would be more sensitive to the disturbances with longer azimuthal wavelengths than to any highly oblique disturbances. The formation of the disturbance peak around $f \approx 168$ kHz as the axial location is increased can be seen in the power spectrum density of the wall pressure and heat-flux fluctuations shown in Figure 15.

Next, we examine the spatial structure of the temperature fluctuations in the vicinity of $f = 167$ kHz. To that end, the temperature fluctuations are bandpass filtered to a single Fourier bin centered on the frequency of interest. The contours of the resulting temperature fluctuations normalized by the mean wall temperature (i.e., T'/T_w) are displayed in Figure 16. The contours are plotted both in the $x - r$ plane and for selected axial locations in the $y - z$ plane. Neither

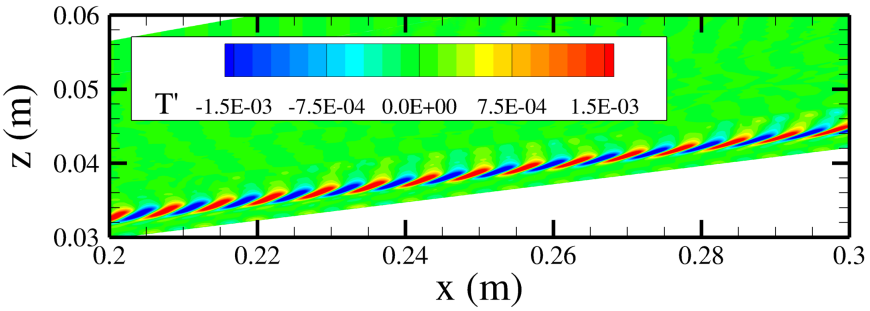

(a) DNS

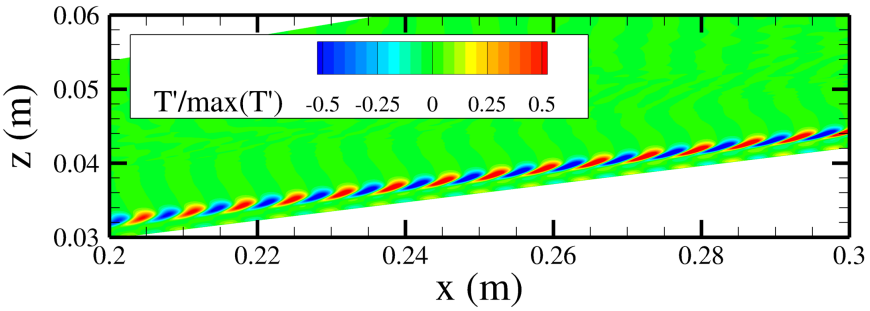

(b) Nonmodal Analysis

Fig. 12 Temperature fluctuations T'/T_w with $f = 150$ kHz predicted by two-dimensional axisymmetric DNS of the Mach 8 cone of $R_n = 5.2$ mm in comparison with the optimal disturbances from the nonmodal analysis.

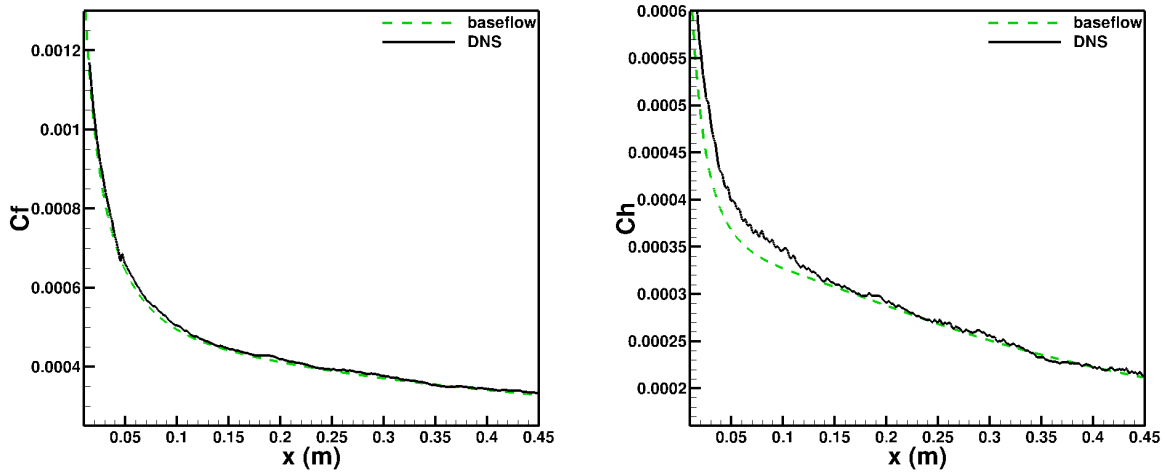

(a) (b)

Fig. 13 (a) Skin-friction coefficient and (b) Stanton number over the Mach 8 cone of $R_n = 5.2$ mm predicted by three-dimensional DNS with tunnel-like acoustic input in comparison with the baseflow.

of these solutions have been Fourier decomposed in the azimuthal direction. The disturbance shape shows strong similarities with the $f = 150$ kHz axisymmetric wave with predicted by the nonmodal analysis as well as with the forced solution excited by planar acoustic waves in the axisymmetric DNS (Figure 12). As shown by the T'/T_w contours in the

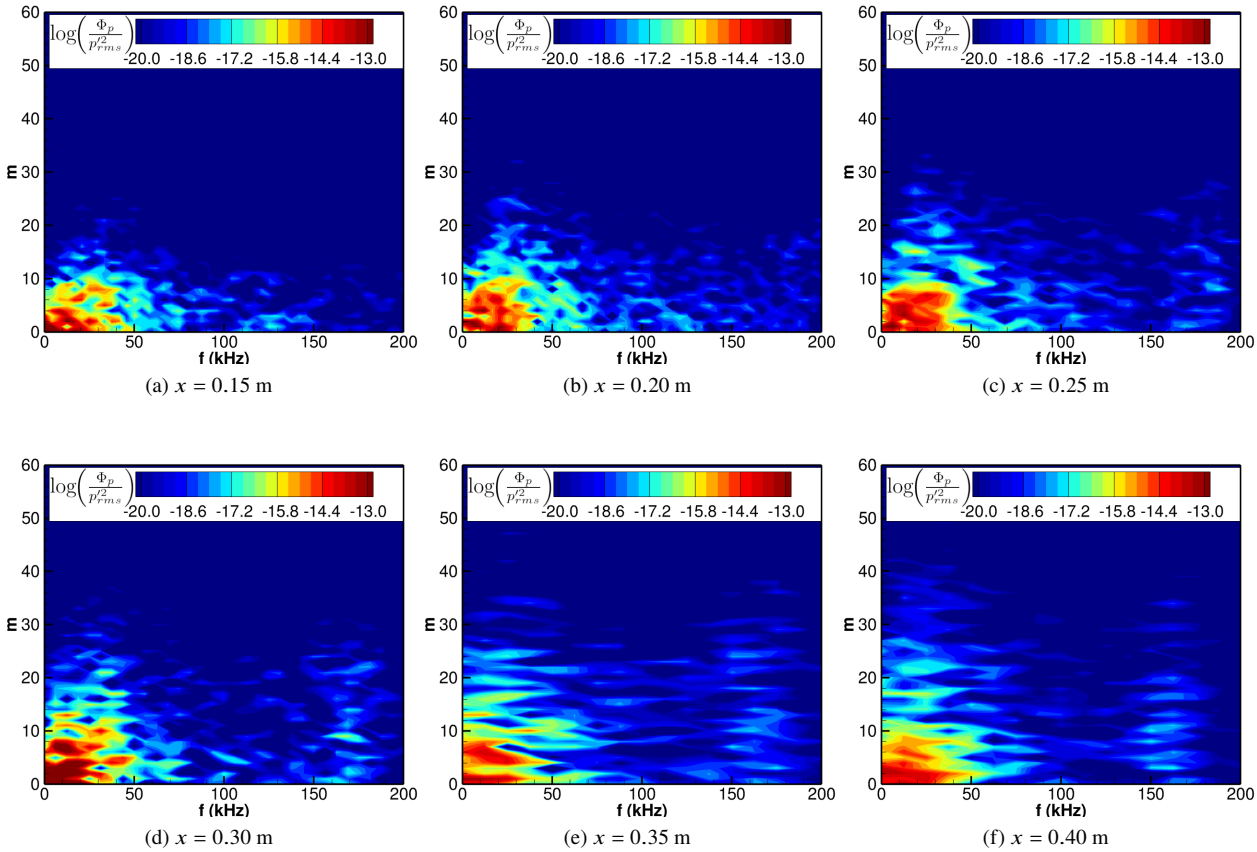

(a) $x = 0.15$ m (b) $x = 0.20$ m (c) $x = 0.25$ m

(d) $x = 0.30$ m (e) $x = 0.35$ m (f) $x = 0.40$ m

Fig. 14 Frequency/azimuthal-wavenumber ($f - m$) spectrum of the wall-pressure fluctuations over the Mach 8 cone of $R_n = 5.2$ mm predicted by three-dimensional DNS with tunnel-like acoustic input.

$y - z$ planes of Figure 16b, the temperature fluctuations are located above the boundary layer edge and show strong variations across the azimuthal direction in the region away from the wall.

The wall-normal variation in the disturbance spectral content is examined next. To that end, the azimuthal wavenumber and frequency spectra of T'/T_w are shown in Figures 17a and 17b, respectively. It may be seen that, in general, only the low azimuthal wavenumber waves penetrate the boundary layer all the way to the near-wall region of the flow. However, the region outside the mean boundary layer displays an additional spectral peak involving strongly oblique waves near $m \approx 125$. This peak occurs at distances of up to 2 times the boundary layer thickness away from the wall. The super harmonic of these oblique disturbances is also present near $m = 250$ and at similar wall-normal locations. The frequency spectrum also shows higher amplitudes across a broad range of frequencies, albeit this peak occurs just beyond the boundary-layer edge, not at $z_n/\delta \approx 2$.

A common observation in schlieren measurements taken during hypersonic boundary layer transition experiments with blunt cones [46, 47] or blunt ogive-cylinder [48] geometries is the appearance of inclined structures that extend above the boundary-layer edge. Computational analysis by Paredes et al. [8, 9] has suggested that the observed disturbances may be associated with the nonmodal amplification of traveling waves. To compare the current solution with the experimental measurements, the time evolution of numerical schlieren contours in the x-r plane is tracked in Figure 18. Of particular interest are the inclined structures that resemble the analogous structures observed in experimental schlieren measurements, indicating that such structures can be excited by the freestream acoustic waves. The convective speed of the structure is approximately equal to the mean flow speed near the edge of the boundary layer. The structure remains nearly unchanged as it gets convected across an axial interval of approximately 0.1 m. A similar structured was tracked in the experimental schlieren measurements of Kennedy et al. [47] for a blunt cone at Mach 6 conditions. The structure was observed to cross the experimental measurement window of nearly the same

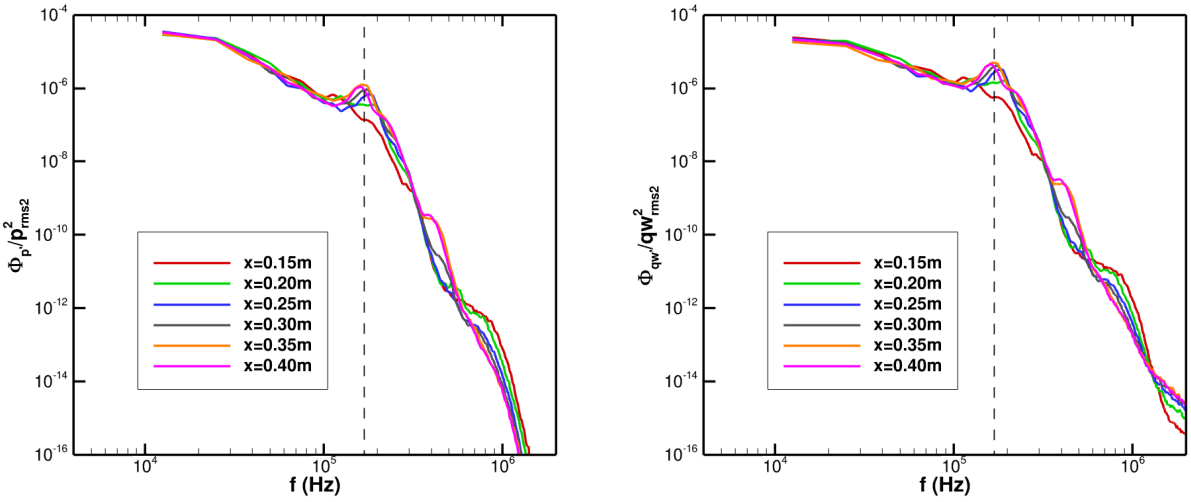

(a) Wall pressure, p_w

(b) Wall heat-flux, q_w

Fig. 15 Power spectrum density of the wall pressure and heat-flux fluctuations over the Mach 8 cone of $R_n = 5.2$ mm predicted by three-dimensional DNS with tunnel-like acoustic input. The dashed line indicates a frequency of $f \approx 168$ kHz.

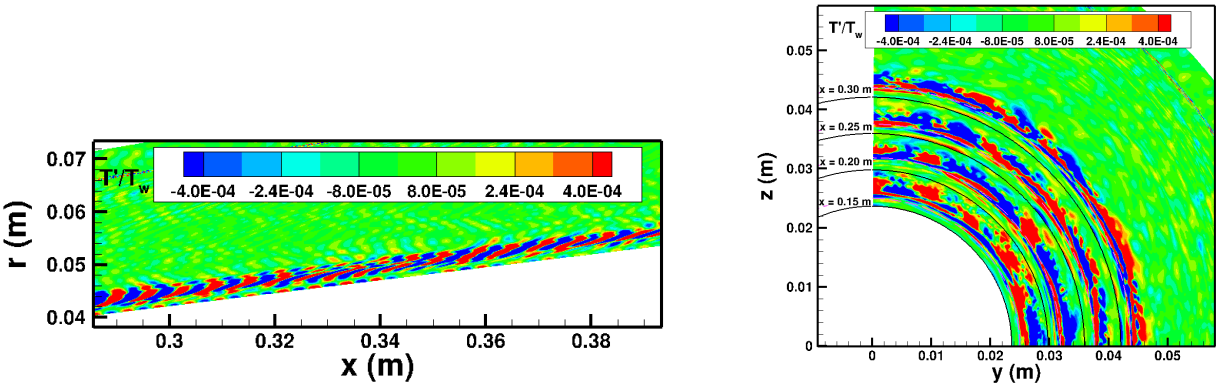

(a) x-r plane

(b) y-z plane

Fig. 16 Temperature fluctuations T'/T_w with $f = 167$ kHz predicted by three-dimensional DNS with tunnel-like acoustic input.

length without any significant changes in form. Although not shown, the analysis of crossplane schlieren contours at successively larger x locations indicates the evolution of the three-dimensional unsteady structures within the entropy layer. Similar to the nonmodal traveling disturbances in the entropy layer [8], these structures are initially located farther from the wall and approach the boundary layer edge as they convect downstream.

Finally, a three-dimensional view of a numerical schlieren isosurface is shown in Figure 19. The isosurface is centered at the axial location of one of the inclined structures discussed above. The figure shows how the plane ($y = 0$) of the numerical schlieren cuts through one of such structures formed above the boundary layer, indicating that the inclined structures observed in the experimental schlieren measurements correspond to three-dimensional structures.

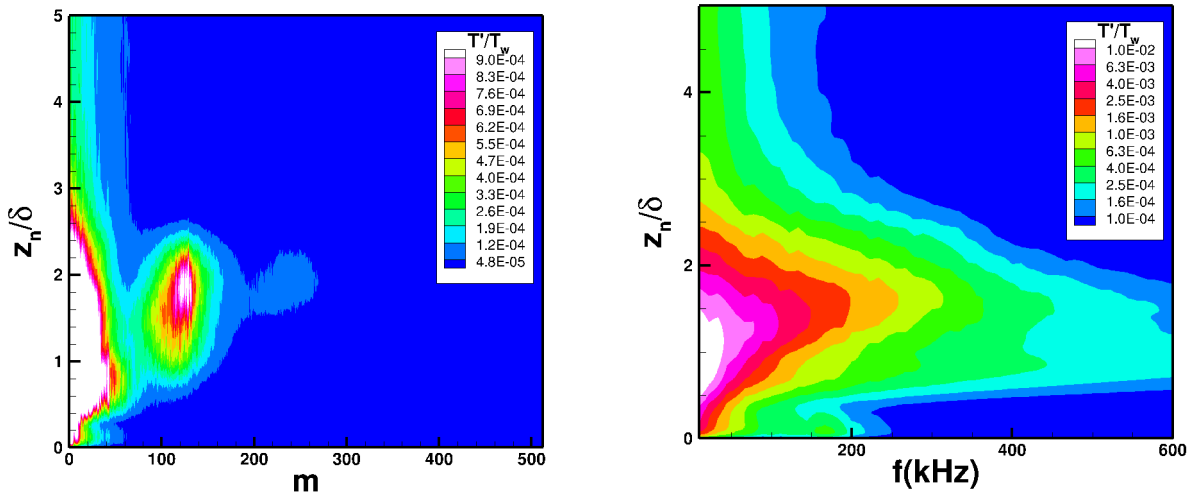

(a) Azimuthal wavenumber spectrum

(b) Frequency spectrum

Fig. 17 Azimuthal wavenumber and frequency spectrum of dimensionless temperature fluctuations T'/T_w along a wall-normal profile at $x = 0.3$ m.

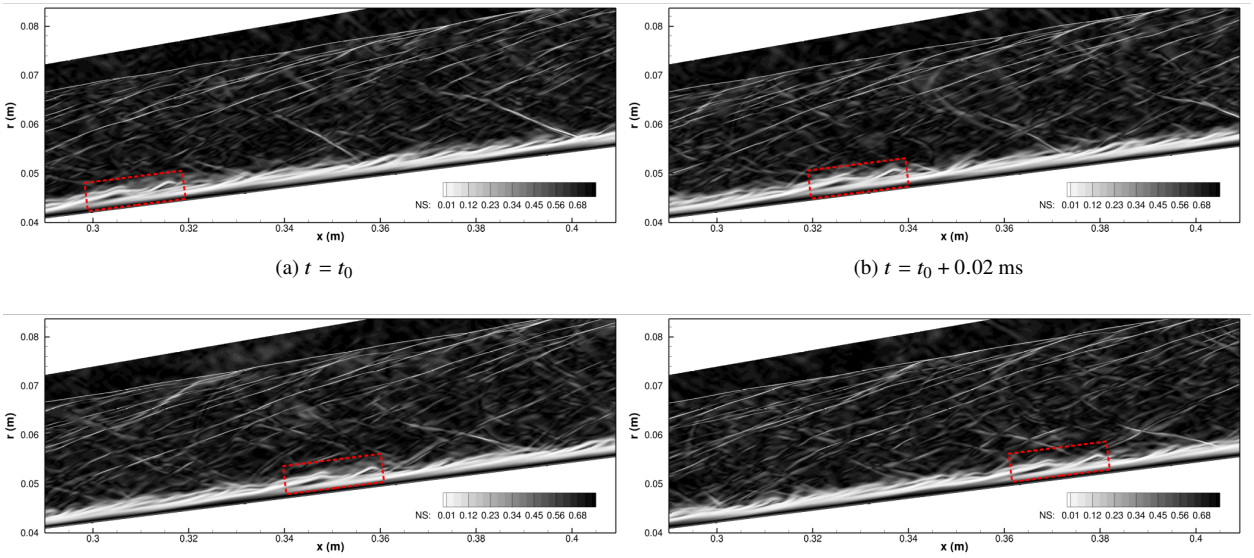

(a) $t = t_0$

(b) $t = t_0 + 0.02$ ms

(c) $t = t_0 + 0.04$ ms

(d) $t = t_0 + 0.06$ ms

Fig. 18 Numerical schlieren (NS) based on the density gradient at different times of the blunt cone.

IV. Summary

In this paper, hypersonic boundary-layer receptivity to broadband freestream acoustic disturbances from the nozzle wall of a digital conventional wind tunnel is investigated by both DNS and stability analysis for Mach 8 flow over a 7 deg half-angle cone with a nose radius of $R_n = 5.2$ mm. The paper first presented a systematic methodology for extracting and reconstructing broadband acoustic disturbances radiated from the nozzle-wall turbulent boundary layer of a conventional hypersonic wind tunnel. The study finds that the broadband tunnel noise in the free stream (i.e., outside of the nozzle-wall turbulent boundary layer) can be well represented by an acoustic model based on a plane wave decomposition comprised of a large number of planar, slow acoustic waves. With successful calibration of the

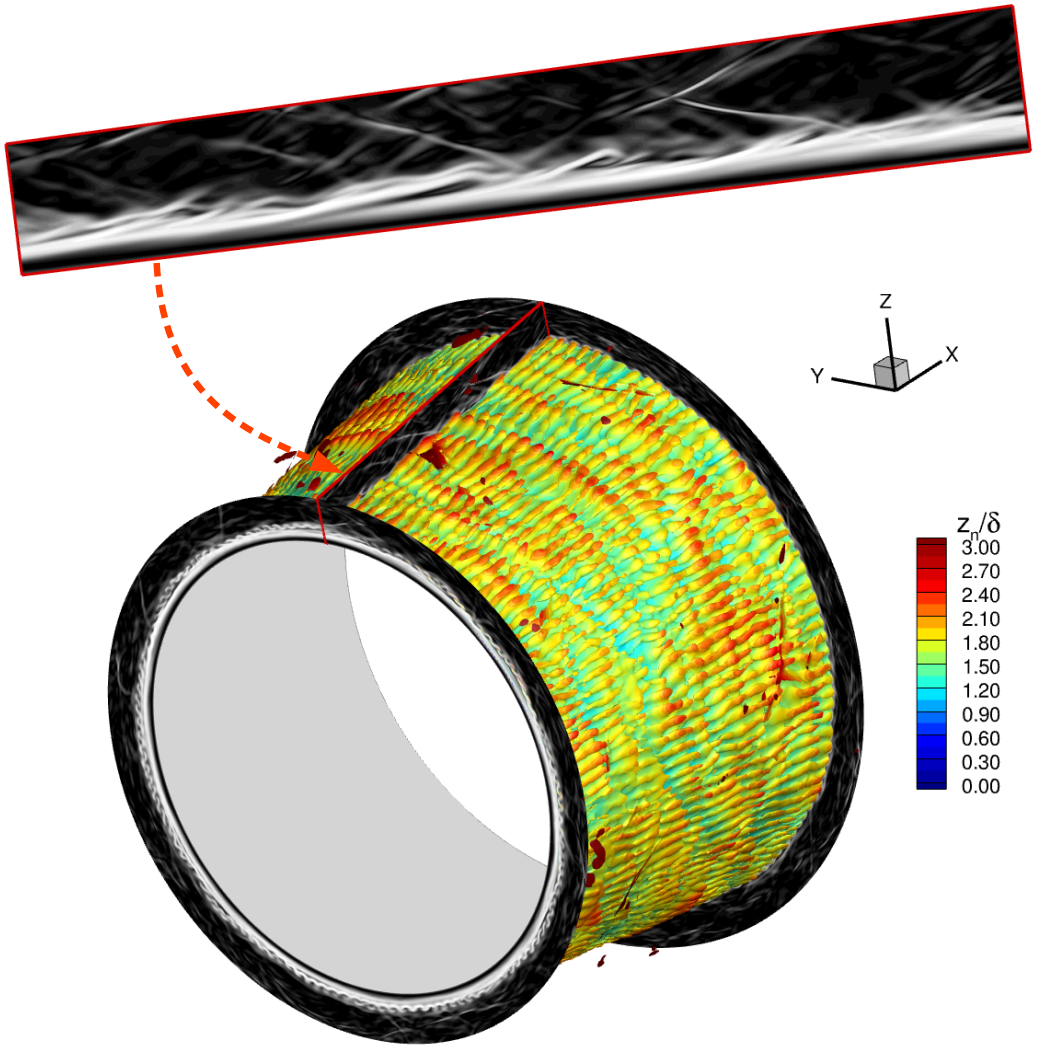

Fig. 19 Isosurface of the numerical schlieren (colored by the dimensionless wall-normal distance z_n/δ) over a cone section of $x = [0.345, 0.423]$ for the Mach 8 cone of $R_n = 5.2$ mm predicted by three-dimensional DNS with tunnel-like acoustic input. The wall distance z_n is normalized by the boundary layer thickness δ at the section start (i.e., $x = 0.345$).

model parameters against the precursor tunnel DNS, the acoustic model can successfully reproduce the frequency and wavenumber spectra of the broadband tunnel noise. Additionally, the temporal evolution of the stochastic acoustic structures is well captured by the calibrated model. Given the analytical nature of the derived acoustic model, the time-series data generated according to such a model can be readily imposed at the outer boundary of a downstream DNS for studying the receptivity and boundary-layer transition phenomena over test articles of other shapes.

Next, the paper presented DNS results of boundary-layer receptivity to freestream acoustic disturbances and the growth of instability waves over a Mach 8 blunt cone with $R_n = 5.2$ mm. The DNS included both two-dimensional axisymmetric DNS with linear freestream acoustic waves and three-dimensional DNS with broadband acoustic disturbances radiated from the tunnel wall, and the results from the DNS were compared with those of the stability analysis.

The axisymmetric DNS study finds that the amplification of Mack's second mode for sharper cones with $R_n = 0.05$ mm and $R_n = 0.5$ mm agrees well with the PSE predictions. For the blunt cone, the stability analysis predicts that

Mack's second mode waves begin to amplify around 0.4 m near the end of the computational domain, but there is significant nonmodal amplification of planar and oblique entropy layer disturbances. Furthermore, the disturbance structures observed from the DNS of axisymmetric disturbances over the blunt cone with $R_n = 5.2$ mm are similar to the nonmodal disturbances predicted by the optimal growth analysis, demonstrating that disturbance structures resembling the nonmodal disturbances can be excited by freestream acoustic disturbances.

The three-dimensional DNS of the Mach 8, $R_n = 5.2$ mm blunt cone with tunnel-like acoustic input above the bow shock predicts a laminar boundary layer throughout the 0.45 m length of the computational domain. The spectra of wall-pressure and heat-transfer fluctuations at $x = 0.4$ m show the signature of axisymmetric as well as moderately oblique waves centered near 168 kHz, similar to the predictions of nonmodal, optimal growth analysis. Furthermore, the azimuthal wavenumber and frequency spectrum of the temperature fluctuations as a function of the wall-normal distance at $x = 0.3$ m show higher amplitudes for three-dimensional waves with an azimuthal wavenumber of approximately 125, at a wall-normal distance of nearly 2.4 times the boundary layer thickness. The frequency spectrum also shows higher amplitudes above the boundary layer thickness. The numerical schlieren contours show the inclined structures commonly observed in blunt cone experiments and demonstrate that they correspond to three-dimensional structures, and can be excited by freestream disturbances in conventional hypersonic experimental facilities in the presence of an entropy layer due to blunt nose tips.

Ongoing and future work includes more detailed data analysis to provide further information regarding the role of the freestream disturbances and the nonmodal growth of traveling disturbances within the entropy layer during the transition process as well as additional DNS runs to cover a longer portion of the cone in order to reach the final breakdown stages of laminar-turbulent transition.

Acknowledgments

Yuchen Liu, Mateus Schuabb, and Lian Duan were supported by the National Science Foundation (under grants CBET 2001125 & 2001127, managed by Dr. Ron Joslin), the Office of Naval Research (ONR) (under grant N00014-17-1-2347, managed by Dr. Eric Marineau), and the Sandia National Laboratory. Pedro Paredes was partially supported by the ONR under grant N00014-20-1-2261, managed by Dr. Eric Marineau, and by the Hypersonic Technology Project (HTP) under the NASA Aeronautics Research Mission Directorate (ARMD). Meelan Choudhari was supported by the HTP under the NASA ARMD. Lian Duan would like to thank Dr. Katya Casper and Dr. Ross Wagnild of Sandia National Laboratory for their wind-tunnel validation data and many valuable discussions. Computational resources were provided by the DoD High Performance Computing Modernization Program and the Ohio Supercomputer Center. The views and conclusions contained herein are those of the authors and should not be interpreted as necessarily representing the official policies or endorsements, either expressed or implied, of the funding agencies or the U.S. Government. The authors report no conflict of interest.

References

[1] Schneider, S. P., "Hypersonic Laminar-Turbulent Transition on Circular Cones and Scramjet Forebodies," *Progress in Aerospace Sciences*, Vol. 40, No. 1-2, 2004, pp. 1–50. https://doi.org/10.1016/j.paerosci.2003.11.001.

[2] Stetson, K., "Nosetip Bluntness Effects on Cone Frustum Boundary Layer Transition in Hypersonic Flow," *AIAA Paper 1983-1763*, 1983. https://doi.org/10.2514/6.1983-1763.

[3] Marineau, E. C., Moraru, C. G., Lewis, D. R., Norris, J. D., Lafferty, J. F., Wagnild, R. M., and Smith, J. A., "Mach 10 Boundary-Layer Transition Experiments on Sharp and Blunted Cones," *AIAA Paper 2014-3108*, 2014. https://doi.org/10.2514/6.2014-3108.

[4] Jewell, J. S., and Kimmel, R. L., "Boundary-Layer Stability Analysis for Stetson'sMach6 Blunt-Cone Experiments," *Journal of Spacecraft and Rockets*, Vol. 54, No. 1, 2017, pp. 258–265. https://doi.org/10.2514/1.A33619.

[5] Jewell, J. S., Kennedy, R. E., Laurence, S. J., and Kimmel, R. L., "Transition on a Variable Bluntness 7-Degree Cone at High Reynolds Number," *AIAA Paper 2018-1822*, 2018. https://doi.org/10.2514/6.2018-1822.

[6] Paredes, P., Choudhari, M. M., Li, F., Jewell, J. S., Kimmel, R. L., Marineau, E. C., and Grossir, G., "Nosetip Bluntness Effects on Transition at Hypersonic Speeds: Experimental and Numerical Analysis Under NATO STO AVT-240," *AIAA Paper 2018-0057*, 2018. https://doi.org/10.2514/6.2018-0057.

[7] Cook, D. A., Thome, J., Brock, J. M., Nichols, J. W., and Candler, G. V., "Understanding Effects of Nose-Cone Bluntness on Hypersonic Boundary Layer Transition using Input-Output Analysis," *AIAA Paper 2018-0378*, 2018. https://doi.org/10.2514/6.2018-0378.

[8] Paredes, P., Choudhari, M. M., Li, F., Jewell, J. S., Kimmel, R. L., Marineau, E. C., and Grossir, G., "Nose-Tip Bluntness Effects on Transition at Hypersonic Speeds," *Journal of Spacecraft and Rockets*, Vol. 56, No. 2, 2019, pp. 369–387. https://doi.org/10.2514/1.A34277.

[9] Paredes, P., Choudhari, M. M., Li, F., Jewell, J. S., and Kimmel, R. L., "Nonmodal Growth of Traveling Waves on Blunt Cones at Hypersonic Speeds," *AIAA Journal*, Vol. 57, No. 11, 2019, pp. 4738–4749. https://doi.org/10.2514/1.J058290.

[10] Paredes, P., Choudhari, M., and Li, F., "Mechanism for Frustum Tranistion over Blunt Cones at Hypersonic Speeds," *Journal of Fluid Mechanics*, Vol. 894, 2020, p. A22. https://doi.org/10.1017/jfm.2020.261.

[11] Goparaju, H., Unnikrishnan, S., and Gaitonde, D. V., "Effects of Nose Bluntness on Hypersonic Boundary-Layer Receptivity and Stability," *Journal of Spacecraft and Rockets*, 2021, pp. 1–17. https://doi.org/10.2514/1.A34829.

[12] Hader, C., and Fasel, H. F., "Towards Simulating Natural Transition in Hypersonic Boundary Layers via Random Inflow Disturbances," *Journal of Fluid Mechanics*, Vol. 847, 2018. https://doi.org/10.1017/jfm.2018.386.

[13] Ran, W., Zare, A., Hack, M. P., and Jovanović, M. R., "Stochastic Receptivity Analysis of Boundary Layer Flow," *Physical Review Fluids*, Vol. 4, No. 9, 2019, p. 093901. https://doi.org/10.1103/PhysRevFluids.4.093901.

[14] Zhong, X., and Ma, Y., "Boundary-Layer Receptivity of Mach 7.99 Flow over a Blunt Cone to Free-Stream Acoustic Waves," *Journal of Fluid Mechanics*, Vol. 556, 2006, p. 55. https://doi.org/10.1017/S0022112006009293.

[15] Balakumar, P., and Chou, A., "Transition Prediction in Hypersonic Boundary Layers using Receptivity and Freestream Spectra," *AIAA Journal*, Vol. 56, No. 1, 2018, pp. 193–208. https://doi.org/10.2514/1.J056040.

[16] Balakumar, P., King, R. A., Chou, A., Owens, L. R., and Kegerise, M. A., "Receptivity and Forced Response to Acoustic Disturbances in High-Speed Boundary Layers," *AIAA Journal*, Vol. 56, No. 2, 2018, pp. 510–523. https://doi.org/10.2514/1.J056145.

[17] Laufer, J., "Aerodynamic Noise in Supersonic Wind Tunnels," *J. Aerosp. Sci.*, Vol. 28, No. 9, 1961, pp. 685–692. https://doi.org/10.2514/8.9150.

[18] Laufer, J., "Some Statistical Properties of the Pressure Field Radiated by a Turbulent Boundary Layer," *Physics of Fluids*, Vol. 7, No. 8, 1964, pp. 1191–1197. https://doi.org/10.1063/1.1711360.

[19] Pate, S. R., "Dominance of Radiated Aerodynamic Noise on Boundary-Layer Transition in Supersonic-Hypersonic Wind Tunnels," Tech. rep., AEDC-TR-77-107, Arnold Engineering Development Center, 1978.

[20] Stetson, K. F., "Nosetip Bluntness Effects on Cone Frustrum Boundary-Layer Transition in Hypersonic Flow," AIAA Paper 1983-1763, 1983. https://doi.org/10.2514/6.1983-1763.

[21] Bushnell, D. M., "Notes on Initial Disturbance Fields for the Transition Problem," *Instability and Transition,* edited by M. Y. Hussaini and R. G. Voigt, Springer-Verlag, Berlin, Vol. 1, 1990, pp. 217–232. https://doi.org/10.1007/978-1-4612-3430-2_28.

[22] Schneider, S. P., "Effects of High-Speed Tunnel Noise on Laminar-Turbulent Transition," *Journal of Spacecraft and Rockets*, Vol. 38, No. 3, 2001, pp. 323–333. https://doi.org/10.2514/2.3705.

[23] Duan, L., Choudhari, M. M., Chou, A., Munoz, F., Ali, S. R. C., Radespiel, R., Schilden, T., Schröder, W., Marineau, E. C., Casper, K. M., Chaudhry, R. S., Candler, G. V., Gray, K. A., and Schneider, S. P., "Characterization of Freestream Disturbances in Conventional Hypersonic Wind Tunnels," *Journal of Spacecraft and Rockets*, Vol. 56, No. 2, 2019, pp. 357–368. https://doi.org/10.2514/1.A34290.

[24] Duan, L., and Martin, M., "An Effective Procedure for Testing the Validity of DNS of Wall-Bounded Turbulence Including Finite-Rate Reactions," *AIAA Journal*, Vol. 47, No. 1, 2009, pp. 244–251. https://doi.org/10.2514/1.38318.

[25] Keyes, F. G., "A Summary of Viscosity and Heat-Conduction Data for HE, A, H_2, O_2, CO, CO_2, H_2O, and Air," *Transactions of the American Society of Mechanical Engineers*, Vol. 73, 1951, pp. 589–596.

[26] Jiang, G. S., and Shu, C. W., "Efficient Implementation of Weighted ENO Schemes," *Journal of Computational Physics*, Vol. 126, No. 1, 1996, pp. 202–228. https://doi.org/10.1006/jcph.1996.0130.

[27] Williamson, J., "Low-Storage Runge-Kutta Schemes," *Journal of Computational Physics*, Vol. 35, No. 1, 1980, pp. 48–56. https://doi.org/10.1016/0021-9991(80)90033-9.

[28] Mohseni, K., and Colonius, T., "Numerical Treatment of Polar Coordinate Singularities," *Journal of Computational Physics*, Vol. 157, 2000, pp. 787–795. https://doi.org/10.1006/jcph.1999.6382.

[29] Bogey, C., de Cacqueray, N., and Bailly, C., "Finite Differences for Coarse Azimuthal Discretization and for Reduction of Effective Resolution Near Origin of Cylindrical Flow Equations," *Journal of Computational Physics*, Vol. 230, 2011, pp. 1134–1146. https://doi.org/10.1016/j.jcp.2010.10.031.

[30] Duan, L., Choudhari, M. M., and Wu, M., "Numerical Study of Acoustic Radiation Due to a Supersonic Turbulent Boundary Layer," *Journal of Fluid Mechanics*, Vol. 746, 2014, pp. 165–192. https://doi.org/10.1017/jfm.2014.116.

[31] Duan, L., Choudhari, M. M., and Zhang, C., "Pressure Fluctuations Induced by a Hypersonic Turbulent Boundary Layer," *Journal of Fluid Mechanics*, Vol. 804, 2016, pp. 578–607. https://doi.org/10.1017/jfm.2016.548.

[32] Huang, J., Zhang, C., Duan, L., and Choudhari, M. M., "Direct Numerical Simulation of Hypersonic Turbulent Boundary Layers Inside an Axisymmetric Nozzle," AIAA Paper 2017-0067, 2017. https://doi.org/10.2514/6.2017-0067.

[33] Huang, J., L. Duan, L., and Choudhari, M. M., "Direct Numerical Simulation of Acoustic Noise Generation from the Nozzle Wall of a Hypersonic Wind Tunnel," AIAA Paper 2017-3631, 2017. https://doi.org/10.2514/6.2017-3631.

[34] Duan, L., Choudhari, M. M., Chou, A., Munoz, F., Ali, S. R. C., Radespiel, R., Schilden, T., Schröder, W., Marineau, E. C., Casper, K. M., Chaudhry, R. S., Candler, G. V., Gray, K. A., Sweeney, C. J., and Schneider, S. P., "Characterization of Freestream Disturbances in Conventional Hypersonic Wind Tunnels," AIAA Paper 2018-0347, 2018. https://doi.org/10.2514/1.A34290.

[35] Duan, L., Nicholson, G. L., Huang, J., Casper, K. M., Wagnild, R. M., and Bitter, N. P., "Direct Numerical Simulation of Nozzle-Wall Pressure Fluctuations in a Mach 8 Wind Tunnel," AIAA Paper 2019-0847, 2019. https://doi.org/10.2514/6.2019-0874.

[36] Balakumar, P., and Kegerise, M. A., "Receptivity of Hypersonic Boundary Layer over Straight and Flared Cones," *AIAA Journal*, Vol. 53, No. 8, 2015, pp. 2097–2109. https://doi.org/10.2514/1.J053432.

[37] Balakumar, P., and Chou, A., "Transition Prediction in Hypersonic Boundary Layers using Receptivity and Freestream Spectra," *AIAA Paper 2016-0847*, 2016. https://doi.org/10.2514/6.2016-0847.

[38] McKenzie, J. F., and Westphal, K. O., "Interaction of Linear Waves With Oblique Shock Waves," *Physics of Fluids*, Vol. 11, 1968, pp. 2350–2362. https://doi.org/10.1063/1.1691825.

[39] Goparaju, H., Liu, Y., Duan, L., and Gaitonde, D. V., "Supersonic Transition Induced by Numerical Tunnel Disturbances," AIAA 2022-1826, 2022. https://doi.org/10.2514/6.2022-1826.

[40] Hildebrand, N., Choudhari, M. M., Deegan, C. P., Huang, J., and Duan, L., "Direct Numerical Simulation of Acoustic Disturbances in a Hypersonic Two-Dimensional Nozzle Configuration," *AIAA Journal*, 2022, pp. 1–12. https://doi.org/10.2514/1.J061053.

[41] Chu, B.-T., "On the Energy Transfer to Small Disturbances in Fluid Flow (PART I)," *Acta Mechanica*, Vol. 1, No. 3, 1965, pp. 215–234. https://doi.org/10.1007/BF01387235.

[42] Casper, K. M., Beresh, S. J., Henfling, J. F., Spillers, R. W., and Pruett, B. O. M., "Hypersonic Wind-Tunnel Measurements of Boundary-Layer Transition on a Slender Cone," *AIAA Journal*, Vol. 54, No. 4, 2016, pp. 1250–1263. https://doi.org/10.2514/1.J054033.

[43] Paredes, P., Choudhari, M., Li, F., and Chang, C.-L., "Optimal Growth in Hypersonic Boundary Layers," *AIAA Journal*, Vol. 54, No. 10, 2016, pp. 3050–3061. https://doi.org/10.2514/1.J054912.

[44] Litton, D., Edwards, J., and White, J., "Algorithmic Enhancements to the VULCAN Navier-Stokes Solver," AIAA Paper 2003-3979, 2003. https://doi.org/10.2514/6.2003-3979.

[45] Marineau, E., Lewis, D., Smith, M., Lafferty, J., White, M., and Amar, A., "Investigation of Hypersonic Laminar Heating Augmentation in the Stagnation Region," AIAA 2013-0308, 2013. https://doi.org/10.2514/6.2013-308.

[46] Grossir, G., Pinna, F., and Chazot, O., "Influence of Nose-Tip Bluntness on Conical Boundary-Layer Instabilities at Mach10," *AIAA Journal*, Vol. 57, No. 9, 2019, pp. 3859–3873. https://doi.org/10.2514/1.J057822.

[47] Kennedy, R., Jewell, J., Paredes, P., and Laurence, S., "Characterization of Instability Mechanisms on Sharp and Blunt Slender Cones at Mach6," *Journal of Fluid Mechanics*, Vol. 936, 2022, p. A39. https://doi.org/10.1017/jfm.2022.39.

[48] Hill, J., Oddo, R. A., Komives, J. R., Reeder, M. F., Borg, M. P., and Jewell, J. S., "Experimental Measurements of Hypersonic Instabilities over Ogive-Cylinders at Mach 6," *AIAA Journal*, 2022, pp. 1–17. https://doi.org/10.2514/6.2021-0153.